JOURNAL OF AIRCRAFT
Vol. 61, No. 1, January–February 2024

Automatic Continuous Thrust Control for Supersonic Transport Takeoff Noise Reduction

Laurens J. A. Voet,* Prakash Prashanth,† Raymond L. Speth,‡ Jayant S. Sabnis,§ Choon S. Tan,¶ and Steven R. H. Barrett**
Massachusetts Institute of Technology, Cambridge, Massachusetts 02139

https://doi.org/10.2514/1.C037394

Advanced takeoff trajectories are proposed for supersonic transport noise reduction by capitalizing on excess engine thrust and improved aerodynamic efficiency at higher takeoff speeds. These novel trajectories use i) automatic continuous control of thrust, ii) increased takeoff speed, and iii) reduced cut-back altitude, compared to conventional pilot-initiated discrete thrust cut-back procedures currently used for subsonic transport. In this paper, we develop an optimal control framework to assess the attributes of effective takeoff trajectories for supersonic transport that yield minimum noise levels. We quantify the noise reduction potential of advanced takeoff trajectories for the eight-passenger, 55-metric-ton, Mach-1.4 NASA Supersonic Technology Concept Airplane. For the aircraft examined, these advanced takeoff trajectories enable a cumulative certification noise reduction of 10.6 EPNdB, which is insufficient to meet current subsonic transport noise limits.

Nomenclature

A_f^*	=	fan inlet area (reference: A_{ref})
A_j^*	=	jet cross-sectional area (reference: A_{ref})
C_L, C_D	=	aircraft aerodynamic lift and drag coefficients
c_0	=	ambient speed of sound, m/s
d_{fan}	=	fan diameter, m
$EPNL$	=	effective perceived noise level, EPNdB
F_n	=	aircraft net thrust, N
$IPNLT$	=	integrated tone-corrected perceived noise level, EPNdB
I_0	=	ambient characteristic impedance, Ω
k_{rot}	=	aircraft rotational speed ratio
L, D	=	aircraft aerodynamic lift and drag forces, N
M_0	=	Mach number
$\dot{m}_{c,i}^*$	=	combustor inlet mass flow (reference: $\rho_0 c_0 A_{\text{ref}}$)
$\dot{m}_f^*$	=	fan inlet mass flow (reference: $\rho_0 c_0 A_{\text{ref}}$)
N_f^*	=	fan rotational speed (reference: c_0/d_{fan})
n	=	aircraft load factor
$PNLT$	=	tone-corrected perceived noise level, TPNdB
$P_{t,c,i}^*$	=	combustor inlet total pressure (reference: p_0)
p_{ref}	=	reference acoustic pressure, Pa
p_0	=	ambient pressure, Pa
$\langle p^2 \rangle^*$	=	mean-square acoustic pressure (reference: p_{ref})
q	=	ambient dynamic pressure, Pa
SEL	=	sound exposure level, dB-A
$T_{t,c,i}^*$	=	combustor inlet total temperature (reference: T_0)
$T_{t,c,j}^*$	=	combustor exit total temperature (reference: T_0)
$T_{t,j}^*$	=	jet total temperature (reference: T_0)
T_0	=	ambient temperature, K
t_s	=	source time, s
V	=	aircraft velocity, m/s
V_j^*	=	ideally expanded jet velocity (reference: c_0)
x, y, z	=	aircraft position, m
α	=	aircraft angle of attack, deg
γ	=	aircraft climb angle, deg
$\Delta T_{t,\text{des},c}^*$	=	turbine total temperature drop at design (reference: T_0)
$\Delta T_{t,f}^*$	=	fan total temperature rise (reference: T_0)
θ_{flap}	=	aircraft flap deflection angle, deg
μ_0	=	ambient dynamic viscosity, kg/ms
ρ_j^*	=	jet density (reference: ρ_0)
ρ_0	=	ambient density, kg/m^3
τ	=	aircraft thrust setting

Presented as Paper 2022-3052 at the 28th AIAA/CEAS Aeroacoustics 2022 Conference, Southampton, England, United Kingdom, June 14–17, 2022; received 17 February 2023; revision received 22 July 2023; accepted for publication 16 September 2023; published online Open Access 4 November 2023.

*Independent Researcher; laurens.ja.voet@gmail.com. Member AIAA (Corresponding Author).
†Postdoctoral Associate, Department of Aeronautics and Astronautics. Member AIAA.
‡Principal Research Scientist, Department of Aeronautics and Astronautics.
§Senior Lecturer, Department of Aeronautics and Astronautics. Fellow AIAA.
¶Senior Research Engineer, Department of Aeronautics and Astronautics. Senior Member AIAA.
**Professor, Department of Aeronautics and Astronautics. Senior Member AIAA.

I. Introduction

THE recently growing interest in second-generation civil supersonic transport (SST) raises concerns about an increase in noise around airports, given the extremely high noise levels of the first-generation Concorde aircraft [1,2]. Recent studies suggest that, with standard takeoff and landing (LTO) procedures, near-term commercial SST is unlikely to meet current existing noise limits for subsonic aircraft, mainly due to the high jet velocities associated with their high-specific thrust propulsion systems [3]. Since Concorde's introduction into service, significant noise reductions have been achieved in subsonic transport by shifting to lower design fan pressure ratio (1.3–1.4) turbofan engines [4,5]. However, the increased engine diameter corresponding to reduced fan pressure ratios results in rapidly rising wave drag at supersonic speeds, leading to increased cruise fuel burn [6]. The opposing requirements for low takeoff noise and cruise fuel burn thus limit possible noise reduction through engine design. Literature therefore suggests that modified takeoff procedures would be necessary for SST to comply with current noise limits for subsonic aircraft [3,7–9]. Such procedures are enabled by variable noise reduction systems (VNRSs), defined as dynamic systems integrated into the aircraft design functioning automatically to change the engine operation or airframe configuration to reduce noise [10]. A programmed thrust cut-back (PTCB) [11] is one example of a VNRS, automatically controlling the engine thrust before reaching the allowable

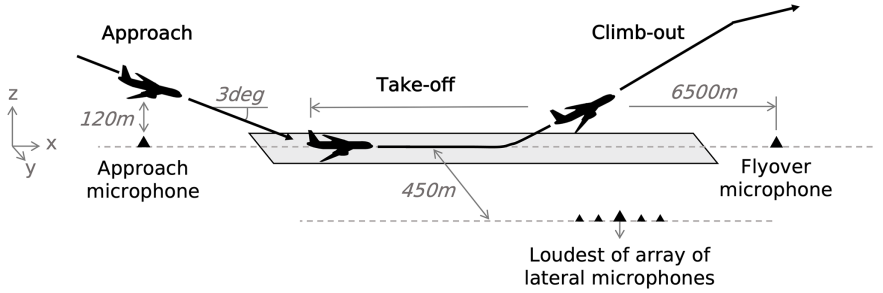

Fig. 1 Sketch of the noise certification microphone arrangement for aircraft takeoff and landing (LTO) operations [12].

pilot-initiated cut-back altitude [12].[††] The PTCB would be programmed in the Full-Authority Digital Engine Control (FADEC) of the engine. Another example of a VNRS is programmed high-lift devices (PHLDs) that automatically control the aircraft flap deflection angles during takeoff, and are programmed directly into the Flight Management System (FMS). However, PHLDs are not considered in this paper. It is proposed that, if such a VNRS is used for noise certification testing, it will also need to be active during normal operations [14]. These automatically actuated and continuously controlled systems are different from the pilot-initiated discrete thrust cut-back procedures currently used for noise certification of subsonic transport.

The design of advanced takeoff trajectories for SST using VNRS falls within the discipline of trajectory optimization with acoustic objective functions, which has been studied extensively in literature. Falck et al. [15] demonstrated the ability to implement acoustic constraints in the trajectory optimization of an urban-air-mobility class aircraft in densely populated areas by treating the aircraft noise source as a single monopole. Further work was suggested by Falck et al. [15] involving the development of a realistic aircraft noise source model coupled to aircraft and engine design parameters. Olson [16] assessed a series of advanced takeoff procedures for the high-speed civil transport AST-105-1 aircraft [17] for community noise reduction on a case-by-case basis. He found that an automatic throttle control with increased rotation velocity and an accelerating climb procedure achieved the best noise reduction. Berton et al. [7] estimated the noise levels of an eight-passenger, Mach-1.4 supersonic business jet using advanced takeoff procedures, in which a grid-search approach was used to assess the effect of PTCB on takeoff noise. The PTCB procedures considered in Berton et al. [7] are characterized by two discrete thrust cut-backs: one initiated by the FADEC and one initiated by the pilot. They found that, through the use of a *discrete* PTCB, the cumulative certification noise levels of an eight-passenger, Mach-1.4, three-engine business jet can be reduced up to ∼1.0 EPNdB above the Chapter 14 limit for subsonic aircraft when using a 10% de-rate on the engines at takeoff [18]. Despite the limited flexibility in optimizing approach trajectories [19], trajectory optimization for noise minimization has been considered for landing operations using analytical noise cost functions [20–24].

No previous work has considered the optimization of SST takeoff trajectories using *automatic continuous thrust control schedules* to minimize takeoff noise levels. It is hypothesized that continuous VNRS can further reduce takeoff certification noise levels by exploiting their increased degrees of freedom compared to the currently used pilot-initiated discrete thrust cut-backs. This paper develops advanced takeoff trajectories for SST noise reduction around airports. While *community* noise reduction is the main objective of such advanced takeoff trajectories, it is not a scalar metric that can readily be optimized as it has a high spatial dependence. Therefore, the ICAO *certification noise* metric (illustrated in Fig. 1) is taken as a surrogate measure of noise exposure around the airport. The metric combines noise measurements at an approach, lateral, and flyover microphones. The approach microphone is not used in this paper, as the focus is on takeoff trajectories. The objectives of this paper are to a) identify attributes of advanced takeoff trajectories for SST using VNRS yielding minimum noise levels, and b) quantify their noise reduction potential.

While an exhaustive search approach can be effective to optimize the control variables in a single thrust cut-back maneuver (i.e., the altitude and amount of thrust cut-back), such an approach quickly becomes computationally intractable when optimizing automatic continuous thrust control schedules [25]. Gradient-based optimization methods enable the design of such VNRS at reduced computational cost. In this paper, an optimal control framework is developed using NASA's OpenMDAO package [26] to design VNRS for takeoff noise minimization. The optimal control framework couples the pyNA aircraft noise estimation model—developed by Voet et al. [27]—to a takeoff trajectory model developed using the Dymos package within NASA OpenMDAO [28]. The optimal control framework uses the sensitivities of acoustic objective functions with respect to engine control variables provided by pyNA to enable effective gradient-based optimization of the thrust control variables along the takeoff trajectory.

The paper is set out as follows: Section II defines the characteristics of advanced takeoff trajectories compared to a standard trajectory abiding by the noise certification standards for subsonic transport in ICAO Annex 16 Volume I [12]. Section III presents the physical models for the aircraft and engine configuration, the takeoff trajectory, and the noise assessment. The formulation of the trajectory optimization problem is outlined in Sec. IV. Section V presents and discusses the results for the advanced takeoff trajectories for the eight-passenger Mach 1.4 NASA Supersonic Technology Concept Aeroplane (STCA) [29].

II. Definition of Standard and Advanced Takeoff Trajectories

Table 1 defines a *standard* trajectory as one that abides by the noise certification regulations for subsonic transport in ICAO Annex 16 Volume I [12]. The key characteristics of the standard

Table 1 Comparison of advanced takeoff trajectory to a standard takeoff trajectory abiding by the ICAO Annex 16 Volume I noise certification regulations for subsonic transport [12]

Parameter	Standard trajectory	Advanced trajectory
Trajectory controls	Pilot-initiated discrete single thrust cut-back	Automatic continuous programmed thrust cut-back
Control altitude	3 engines: $z_{cb} > 260$ m (853 ft) 4 engines: $z_{cb} > 210$ m (689 ft)	$z_{cb} > 10.7$ m (35 ft)
Takeoff speed	$V_2 + 5.1$ m/s (10 kts) $< V_{TO} < V_2 + 10.3$ m/s (20 kts)	$V_{TO} < 128.6$ m/s (250 kts)

[††]Advanced takeoff procedures using automatic thrust control for community noise abatement were first proposed during the Supersonic Cruise Research program by Grantham and Smith [13] to reduce noise at the lateral microphone. In literature, such a takeoff procedure has become known as autothrottle or programmed lapse rate (PLR) [7]. In this paper, the authors propose the term *programmed thrust cut-back* (PTCB) instead of PLR because the term *lapse* implies a degradation in thrust due to phenomena other than a deliberate fuel flow reduction, including changes in flight Mach number and ambient conditions. As such, a PTCB is an advanced procedure compared to the standard single-thrust cut-back (STCB) procedure initiated by the pilot.

takeoff trajectory regarding trajectory controls and operational space are as follows:

1) *Trajectory controls*: ICAO Annex 16 Volume I App. 2 §8.1.1.2 (a) [12] defines the trajectory controls as a pilot-initiated single thrust cut-back (STCB). In this paper, the high-lift device deflection angles are fixed during the takeoff trajectory, i.e., PHLDs are not considered. The STCB is assumed to be a discrete maneuver; i.e., the cut-back time scale ($\mathcal{O}(1)$ s) is significantly shorter compared to the trajectory time scales ($\mathcal{O}(10)$ s).

2) *Control altitude*: ICAO Annex 16 Volume I §3.6.2 (a) [12] specifies that a minimum height must be reached before engine cutback can be initiated by the pilot. This minimum height is 260 m for a three-engine aircraft and 210 m for a four-engine aircraft.

3) *Takeoff speed*: ICAO Annex 16 Volume I §3.6.2 (d) [12] defines that the all-engine operating takeoff climb speed should be between $V_2 + 5.1$ m/s (10 kts) and $V_2 + 10.3$ m/s (20 kts), where V_2 is the takeoff safety speed. This takeoff speed shall be attained as soon as practicable after liftoff.

The propulsion systems of the second generation SST currently being developed are low or medium bypass turbofans (i.e., a design fan pressure ratio ~2), instead of the afterburning Olympus 593 turbojet engines used on Concorde. These engines are likely to have excess thrust capability at the takeoff condition, as they are designed for the (supersonic) top-of-climb condition. This excess thrust can enable effective PTCB schedules for noise reduction. Furthermore, SST employs delta wings as opposed to high aspect ratio wings for subsonic transport. Such delta wings have poor aerodynamic efficiency ($L/D \sim 6$–7) at low speeds. Higher takeoff speeds can enable improved climb performance and thereby reduce noise on the ground. Additionally, higher takeoff speeds can reduce the source noise of the jet mixing noise dominant SST engines by reducing the shear between the jet and the ambient velocity.

The *advanced* takeoff trajectories employ one or a combination of modifications to the trajectory controls, the control altitude, and takeoff speed compared to the standard trajectory, based on the aforementioned unique characteristics of SST. The key characteristics of the advanced takeoff trajectories are as follows:

Table 2 NASA STCA propulsion system thrust demand targets [29]; top-of-climb sets the engine sizing point as the mission most demanding operating point

Mission parameter	Sea level static (SLS)	Takeoff (TO)	Top-of-climb (TOC)	Start of cruise (SOC)	End of cruise (EOC)
Altitude [km]	0	0	12.5	12.5	15.5
Mach number	0	0.25	1.4	1.4	1.4
Thrust [kN]	73.9	62.9	24.5	21.4	14.7

1) *Trajectory controls*: The advanced takeoff trajectories employ automatic continuous thrust control schedules, i.e., PTCB. In this study, the high-lift devices are kept fixed during the takeoff trajectory.

2) *Control altitude*: 14 CFR 25, §25.111 [30] defines an obstacle clearance height of 10.7 m (35 ft) above ground level. The minimum control altitude is reduced to this altitude to be able to affect sideline noise at low altitudes (above 10.7 m and below 260 or 210 m for three- or four-engine aircraft, respectively). By selecting 10.7 m (35 ft) as the minimum control altitude, the takeoff field distance is unaffected.

3) *Takeoff speed*: A maximum takeoff speed of 128.6 m/s (250 kts) below 3048 m (10,000 ft) altitude is defined in the general operating and flight rules (14 CFR §91.117.a [31]). The maximum takeoff speed is increased to this limit to enable SST to take off with increased aerodynamic efficiency.

The modifications to the trajectory controls, control altitude, and takeoff speed listed above have been taken from a combination of aircraft regulations (Part 25—Airworthiness Standards: Transport Category Airplanes; Part 36—Noise Standards: Aircraft Type and Airworthiness Certification; Part 91—General Operating and Flight Rules) to form a set of mathematical constraints for the takeoff procedure for the STCA.

III. Physical Models

A. Aircraft and Engine Configuration

Advanced take-off trajectories for noise reduction are developed for the STCA, designed by NASA in service of International Civil Aviation Organization (ICAO) studies to assess environmental and economic impacts of SST [29]. A solid model representation of the STCA airframe can be found in the work of Berton et al. [29]. The NASA STCA is a 55-metric-ton, eight-passenger business trijet equipped with a delta wing, designed with a transatlantic range (4240 nm), and cruising at Mach 1.4 at altitudes between 12.5 and 15.5 km [29].

The NASA STCA is equipped with a derivative engine for its propulsion system, repurposing its engine core from an existing donor engine. In this paper, a model of a CFM56-5B derivative engine for the NASA STCA business jet is developed using the Numerical Propulsion System Simulation (NPSS) software [32]. The model of the CFM56-5B donor engine is validated using the thrust versus fuel flow characteristic, available in the ICAO Engine Emission Databank [33]. Subsequently, a purpose-designed low-spool is designed around the donor core to meet the STCA mission thrust demand targets (Table 2). Details of the derivative engine model development can be found in Prashanth et al. [34].

B. Takeoff Trajectory Model

The aircraft takeoff trajectory is illustrated in Fig. 2 and consists of five phases: ground roll, rotation, liftoff, automatic and continuous thrust control, and cut-back. Table 3 summarizes the state variables,

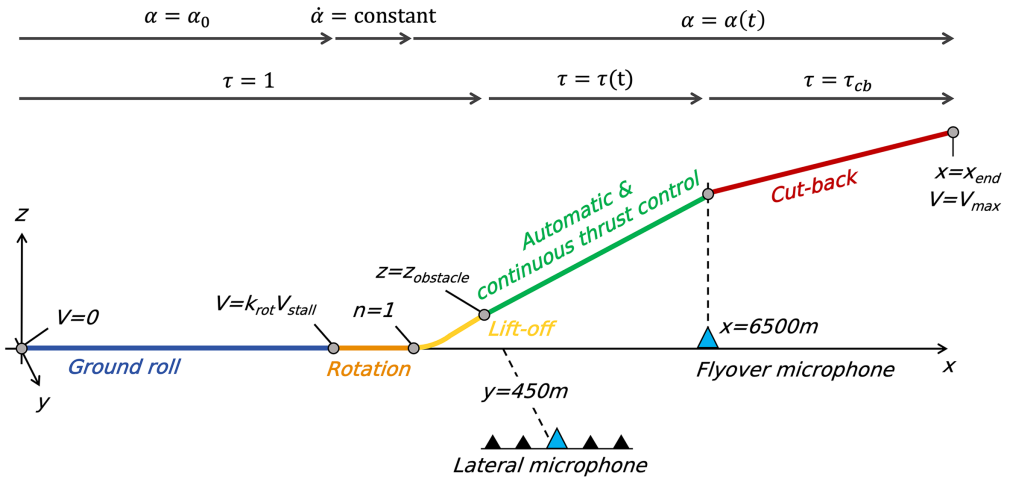

Fig. 2 Takeoff trajectory definition indicating its five consecutive phases, including boundary constraints and control variables.

Table 3 Definition of advanced takeoff trajectories using automatic and continuous thrust as a combination of five phases with states, boundary constraints, path constraints, and trajectory controls

Phase	States	Boundary constraints	Path constraints	Controls: Angle of attack	Controls: Thrust
Ground roll	x, v	Initial: $V_i = 0$ Final: $V_e = k_{\text{rot}} V_{\text{stall}}$		α_0	$\tau = 1$
Rotation	x, v	Initial: $\alpha_i = \alpha_0$ Final: $n_e = 1$		$\frac{d\alpha}{dt} = 3.5$ deg/s	$\tau = 1$
Liftoff	x, z, v, γ	Initial: $z_i = 0$ Final: $z_e = z_{\text{obstacle}}$	$\dot{\gamma} \geq 0$	$\alpha(t)$	$\tau = 1$
Automatic and continuous thrust control	x, z, v, γ	Initial: $z_i = z_{\text{obstacle}}$ Final: $x_e = x_{\text{flyover}}$	$\dot{V} \geq 0$ $\begin{cases} \gamma \geq 0 & \text{if OEI} \\ \gamma > 4\% & \text{else} \end{cases}$	$\alpha(t)$	$\tau(t)$
Cut-back	x, z, v, γ	Initial: $x_i = x_{\text{flyover}}$ Final: $x_e = x_{\text{end}}$ Final: $V_e = V_{\text{max}}$	$\dot{V} \geq 0$ $\begin{cases} \gamma \geq 0 & \text{if OEI} \\ \gamma > 4\% & \text{else} \end{cases}$	$\alpha(t)$	τ_{cb}

boundary constraints, path constraints, and control variables for the respective five phases.

In the *ground roll phase*, the aircraft accelerates until rotation speed, keeping the angle of attack α and thrust setting τ constant. The engine thrust setting is defined as the ratio of applied net thrust compared to the maximum thermodynamically available net thrust at a flight condition and at 100% high-spool speed. The rotation speed is defined as a multiple of the aircraft stall speed, i.e., $V_{\text{rot}} = k_{\text{rot}} V_{\text{stall}}$. The rotation speed ratio k_{rot} is a control parameter that is optimized in order to meet the final velocity boundary constraint, as well as to reduce noise levels.[‡‡] A constant rotation rate, $\dot{\alpha} = 3.5$ deg/s [35], is applied in the *rotation phase* until the aircraft load factor, $n = 1$, is obtained. Subsequently, the aircraft climbs in the *liftoff phase* on a curved path until the runway obstacle clearance height $z_{\text{obstacle}} = 10.7$ m (35 ft) is reached, at which point the landing gear is retracted. The angle of attack is controlled as a continuous function of time to meet the path constraint, i.e., maintaining a positive rate of change of the climb angle. After the obstacle height is cleared, the *automatic and continuous thrust control* is enabled, $\tau = \tau(t)$. Once the location of the flyover observer is reached ($x = 6500$ m, where x is the distance past brake release), the thrust setting is kept constant in the *cut-back phase* equal to the cut-back thrust setting τ_{cb}. The cut-back phase ends at $x = 15,000$ m past the brake-release point. During the liftoff, automatic and continuous thrust control, and cut-back phases, the angle of attack is controlled as a continuous function of time to maintain a positive rate of change in the airspeed. The automatic and continuous thrust control and cut-back phases are also constrained by a minimum 4% climb gradient requirement as well as a steady-level flight requirement with one-engine-inoperative (OEI), whichever requires more thrust (ICAO Annex 16 Volume I §3.6.2.b [12]). It is assumed that the aircraft thrust reduces by one third at OEI, i.e., a change in the aircraft thrust requirement because of the yaw moment rudder increment corresponding to OEI is neglected. Finally, the flap deflection angle is kept constant along the trajectory, as the design of PHLDs is beyond the scope of this paper.

The takeoff trajectory model is developed using NASA Dymos [28] within NASA OpenMDAO [26]. NASA OpenMDAO is an open-source framework making use of, among others, analytic derivatives to develop efficient multidisciplinary analysis and optimization tools. The framework has been used for a wide range of applications, including trajectory optimization, wing design, and structural topology optimization. The NASA Dymos package is a library within NASA OpenMDAO for optimizing control schedules for dynamic systems. Specifically, the package enables optimal control of systems constructed with ordinary differential equations (ODEs). The Flight Optimization System (FLOPS) software designed by NASA [36] was not chosen for the takeoff trajectory model, as it is a stand-alone software that cannot effectively be coupled to aircraft noise estimation models for multidisciplinary design and optimization, as required for this research.

NASA Dymos uses an implicit collocation technique to compute control schedules for dynamic systems in which the states and controls of the dynamic system are approximated using piecewise polynomials (splines) [28]. The coefficients of the polynomials are optimized to satisfy the ODE as well as the path and boundary constraints at a set of discrete collocation points, i.e., drive the defect residuals at the collocation points to zero. An alternative to implicit collocation methods is explicit shooting methods. Collocation methods are preferred over explicit shooting methods for performance and robustness reasons, although this depends on the specific problem [28]. Possible performance benefits of collocation methods can be attributed to the sparsity of their Jacobian matrices, while their improved robustness can be attributed to the decoupling of the state and control history compared to shooting methods [37].

Each phase of the trajectory is discretized using a Gauss–Lobatto pseudo-spectral transcription method [38] characterized by a number of segments, n_{seg}, and a transcription order n_{order}. A trajectory solution that is continuous in its first derivative is selected. Furthermore, as the Gauss–Lobatto transcription requires an odd number of points, the minimum transcription order for the collocation of the state and control variables is 3. The number of segments is varied in each phase to ensure a time step $\Delta t < 0.5$ s. This requirement is set by Annex 16 Volume I [12] to yield sufficient temporal resolution for the time integration of tone-corrected perceived noise level (*PNLT*) in the effective perceived noise level (*EPNL*) calculation.

The trajectory model computes the rates of change of the flight dynamics state variables $\dot{x}$, $\dot{z}$, $\dot{v}$, $\dot{\alpha}$, and $\dot{\gamma}$ using various modules to evaluate the atmospheric properties, aerodynamic performance, and propulsion characteristics. The inputs and outputs of the governing equations of the individual modules in the takeoff trajectory model are illustrated using an extended design structure matrix (XDSM) in Fig. 3 [39]. The rates of change are implicitly integrated using the Dymos package to obtain the time series of the state variables as well as the control variables. A detailed description of the governing equations in the modules of the takeoff trajectory model is given in Appendix A.

C. Noise Model

The pyNA aircraft noise estimation model [27] is used to compute the noise levels at the takeoff certification microphones. To the best of the authors' knowledge, pyNA is the only model that provides sensitivities of aircraft acoustic metrics to engine design and control variables, thus enabling multidisciplinary optimization and optimal control for low-noise aircraft. The flyover microphone

[‡‡]The use of the rotation speed ratio is a low-fidelity method to model the balanced field distance requirement with one-engine-inoperative, described in 14 CFR Part 25.

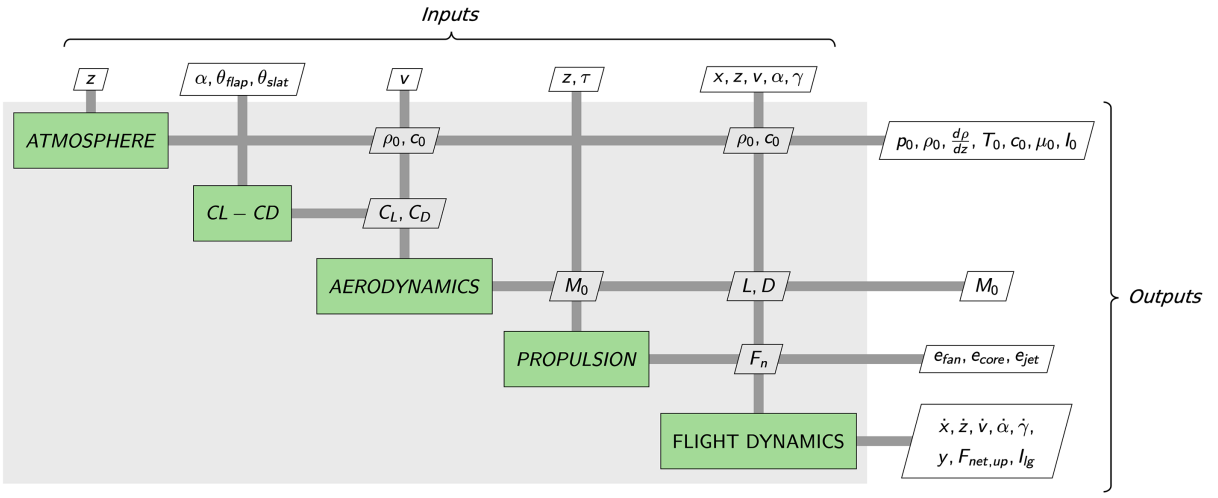

Fig. 3 Extended design structure matrix (XDSM) of the trajectory model showing the relation between inputs and outputs of its modules.

is fixed underneath the flight path at 6500 m downstream of the brake-release point, whereas the lateral microphone is placed on a 450 m lateral sideline, at the position resulting in maximum lateral noise [12].

The methods from the literature used to model the individual noise sources, the noise propagation from the source to the observer, and the certification noise level computation at the observer are summarized in Table 4. The engine and airframe noise sources are assumed to be compact for far-field noise propagation between the takeoff trajectory and the certification microphones. The effect of engine noise shielding by the airframe has been neglected, meaning that forward radiated fan broadband and tonal noise are likely to be overpredicted in this paper. SAE AIR-5662 [50] uses a post hoc subtraction from the aircraft noise levels to account for lateral attenuation effects at low elevation angles. As the post hoc subtraction is applied to the noise levels, it is thus not dependent on one-third octave band frequency. More details about the pyNA aircraft noise estimation model, including its XDSM diagram, can be found in Voet et al. [27].

The utility of the pyNA aircraft noise estimation model is assessed against the NASA ANOPP noise assessment of the NASA STCA on a standard takeoff trajectory [29]. Note that pyNA is able to accurately compute aircraft noise levels at multiple microphone locations near the takeoff trajectory. Specifically, a maximum difference between pyNA and NASA ANOPP of +0.1 EPNdB is found for the total $EPNL$, governed by the good agreement for the jet mixing noise source module [27].

Table 4 Summary of the methods from literature used in the aircraft noise estimation model

Module	Method
Noise source modules	
Fan broadband and tones	Heidman method [40] with • GE Aircraft Engines revision for broadband noise [41] • Allied Signal revision for rotor-stator tones [42] • GE Aircraft Engines fan liner treatment method [43]
Core	Emmerling method [44]
Jet mixing	SAE ARP876: Single-stream, shock-free jet mixing noise [45]
Airframe	Recalibration of Fink method [46] using high-speed research (HSR) method [47]
Noise propagation modules	
Spherical spreading, characteristic impedance, and frequency shift for moving observers	Inverse squared distance law, characteristic impedance ratio, and Doppler effect
Atmospheric absorption	Exponential decay using atmospheric absorption coefficient [48]
Ground reflection and attenuation	Chien–Soroka method [49]
Lateral attenuation	SAE AIR 5662 [50]
Noise levels modules	
Perceived noise level, tone corrected (*PNLT*)	ICAO Annex 16 Volume I [12]
Effective perceived noise level (*EPNL*)	ICAO Annex 16 Volume I [12]

IV. Optimization Problem Formulation

A. Optimal Control Framework

The objective of the automatic continuous thrust control system is to minimize the noise levels at both the lateral and flyover microphones, i.e., $EPNL_{\text{lateral}}$ and $EPNL_{\text{flyover}}$. This multi-objective optimization problem is cast as an optimization problem with a single composite objective function in Eq. (1) minimizing the takeoff noise level, $EPNL_{\text{take-off}} = EPNL_{\text{lateral}} + EPNL_{\text{flyover}}$. The takeoff trajectory model (Sec. III.B) and the aircraft noise estimation model (Sec. III.C) are combined using the NASA OpenMDAO package [26] to solve the optimal control problem:

$$\begin{aligned} \alpha^*(t), \tau^*(t), k^*_{\text{rot}} = \underset{\substack{\alpha \in [\alpha_{\min}, \alpha_{\max}] \\ \tau \in (0,1] \\ k_{\text{rot}} \in [1.1, 1.5]}}{\text{argmin}} \quad & (EPNL_{\text{lateral}} + EPNL_{\text{flyover}}) \\ \text{subject to} \quad & \text{boundary and path constraints (Table 3)} \end{aligned} \tag{1}$$

The control variables are the angle of attack $\alpha(t)$ the thrust-setting schedule in the automatic and continuous thrust control phase, $\tau(t)$, as well as the rotation speed ratio k_{rot}. The lower bound on the rotation speed ratio is to meet the minimum unstick speed requirement $V_{\text{MU}} > 1.1V_{\text{rot}}$ [35]; the upper bound is selected to avoid takeoff speeds above $V_{\max} = 128.6$ m/s (250 kts). The tire operating speed provides an additional (practical) upper bound constraint on the rotation speed ratio; commercial subsonic aircraft have a maximum tire speed between ~113 and 120 m/s (220 and 235 kts), Concorde had a maximum tire speed of 125 m/s (242.4 kts) [51]. It is assumed that sufficient runway length is available for the aircraft to accelerate. The extended design structure matrix (XDSM) of the optimal control framework is shown in Fig. 4 [39]. Given the control variables, $X_{\text{control}} = \{\alpha(t), \tau(t), k_{\text{rot}}\}$, the trajectory module computes the flight path $\{t_s, x, y, z, v, \alpha, \gamma\}$ and engine operating variables $\{Y_{\text{fan}}, Y_{\text{core}}, Y_{\text{jet}}\}$ along the trajectory. The engine operating variables serve as inputs to the pyNA fan, core, and jet noise models, and are given by the sets in Eq. (2):

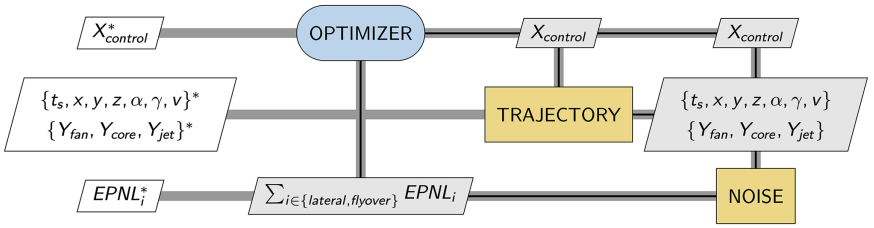

Fig. 4 Extended design structure matrix (XDSM) of the noise-optimal control framework as combination of the trajectory and noise model.

$$\begin{cases} Y_{\text{fan}} = \{\Delta T t_f^*, \dot{m}_f^*, N_f^*\} \\ Y_{\text{core}} = \{\dot{m}_{c,i}^*, T_{t,c,i}^*, T_{t,c,j}^*, P_{t,c,i}^*, \Delta T_{t,\text{des},c}^*\} \\ Y_{\text{jet}} = \{V_j^*, \rho_j^*, A_j^*, T_{t,j}^*\} \end{cases} \tag{2}$$

Then, given an array of observer locations, the noise module uses these flight paths and engine operational variables to compute the takeoff certification noise level, $EPNL_{\text{take-off}} = EPNL_{\text{lateral}} + EPNL_{\text{flyover}}$. The optimal control framework employs the gradient-based interior point optimization algorithm —implemented in the Interior Point Optimizer (IPOPT; Version 3.13.1) package [52]—to optimize for the control variables. The noise-optimal control schedule along the trajectory, X^*_{control}, is determined using the sensitivities of $EPNL$ with respect to the trajectory control variables X_{control}. This sensitivity is decomposed using the chain rule as given in Eq. (3):

$$\frac{\partial EPNL_{\text{take-off}}}{\partial X_{\text{control}}} = \underbrace{\left(\sum_i \underbrace{\frac{\partial Y_{\text{engine},i}}{\partial X_{\text{control}}}}_{\text{Engine response}} \cdot \underbrace{\frac{\partial EPNL_{\text{take-off}}}{\partial Y_{\text{engine},i}}}_{\text{Noise response}} + \sum_j \underbrace{\frac{\partial Y_{\text{airframe},j}}{\partial X_{\text{control}}}}_{\text{Airframe response}} \cdot \underbrace{\frac{\partial EPNL_{\text{take-off}}}{\partial Y_{\text{airframe},j}}}_{\text{Noise response}} \right)}_{\text{Term I: Noise generation}} + \underbrace{\sum_k \left(\underbrace{\frac{\partial Y_{\text{flight path},k}}{\partial X_{\text{control}}}}_{\text{Trajectory response}} \cdot \underbrace{\frac{\partial EPNL_{\text{take-off}}}{\partial Y_{\text{flight path},k}}}_{\text{Noise response}} \right)}_{\text{Term II: Noise propagation}} \tag{3}$$

The sensitivities of the engine operating variables, $\partial Y_{\text{engine},i}/\partial X_{\text{control}}$, are computed using analytical partial derivatives of a third-order Lagrange polynomial interpolation from the NPSS engine deck of the derivative engine model. If the aircraft employed PHLDs, the airframe sensitivities $\partial Y_{\text{airframe},j}/\partial X_{\text{control}}$ would be equal to 1 for control variables of the high-lift devices and 0 for engine control variables. The trajectory sensitivities, $\partial Y_{\text{flight path},k}/\partial X_{\text{control}}$, are computed analytically and implemented explicitly in the Dymos trajectory model. The noise sensitivities $\partial EPNL_{\text{take-off}}/\partial Y_{\text{engine},i}$, $\partial EPNL_{\text{take-off}}/\partial Y_{\text{airframe},j}$, and $\partial EPNL_{\text{take-off}}/\partial Y_{\text{flight path},k}$ are computed in pyNA using the Julia ReverseDiff automatic differentiation package [53].

Term I in Eq. (3) governs how both engine and airframe control parameters affect the noise generation at the source, while Term II governs how those control variables affect the noise propagation between the source and the observers by changing the trajectory. As an example, Eq. (4) shows the sensitivity of takeoff $EPNL$ with respect to engine thrust setting τ by examining the dominant terms in the expansion of Eq. (3):

$$\frac{\partial EPNL_{\text{take-off}}}{\partial \tau} = \underbrace{\frac{\partial V_{\text{jet}}}{\partial \tau} \cdot \frac{\partial EPNL_{\text{take-off}}}{\partial V_{\text{jet}}} + \cancelto{0}{\frac{\partial \theta_{\text{flaps}}}{\partial \tau} \cdot \frac{\partial EPNL_{\text{take-off}}}{\partial \theta_{\text{flaps}}}}}_{\text{Term I: Noise generation}} + \underbrace{\frac{\partial z}{\partial \tau} \cdot \frac{\partial EPNL_{\text{take-off}}}{\partial z}}_{\text{Term II: Noise propagation}} \tag{4}$$

An increase in thrust setting yields an increase in mixed jet velocity, which in turn increases source noise because of increased jet shear. The noise generation term is thus positive. The increase in thrust setting is used to climb and thus yields an increase in flight altitude. This increase in altitude results in an increased propagation distance between the source and the observer, which reduces the takeoff $EPNL$. The noise propagation term is thus negative. Equation (3) shows how the design of continuous control schedules for advanced takeoff trajectories for SST is a trade between noise generation at the source and noise propagation between the source and the observer.

B. Modification of Certification Noise Objective Function for Optimal Control

The optimal control framework presented in Sec. IV.A is used to solve the optimal control problem in Eq. (1). The objective function of the optimal control framework for the advanced takeoff trajectory using PTCB is the takeoff $EPNL$. This section presents four modifications to the takeoff $EPNL$ objective function to enable optimal control using certification noise metrics as the objective function.

The modifications to the takeoff $EPNL$ objective function have been developed on an empirical basis. The IPOPT optimization iteration history provides useful insight into posing the optimization problem in the correct way.[§§] The IPOPT interior point optimization algorithm converges when the following variables fall below a preset tolerance:

1) *Primal infeasibility* denotes the trajectory constraint violation. The convergence to zero of the primal infeasibility indicates that the trajectory is physically feasible and not violating any trajectory constraints.

2) *Dual infeasibility* denotes the trajectory optimality violation for the specified objective function. The convergence to zero of the dual infeasibility thus indicates the optimality of the solution.

The modifications to the acoustic objective functions are defined to achieve convergence of the optimal control problem and thus achieve feasible takeoff trajectories for SST noise reduction.

1. *Pareto Optimality for Multi-Objective Optimization Problem*

The optimal control problem of Eq. (1) with takeoff $EPNL$ as the objective function is a multi-objective optimization problem, i.e., minimizing the sum of the lateral and flyover $EPNL$. As the lateral and flyover objective functions compete with each other, this problem can give rise to Pareto optimality, for which the two subobjectives can be traded while keeping the composite objective function (i.e., the sum of the subobjectives) constant [54]. In the optimization iteration history, such Pareto optimality manifests as a converging primal infeasibility and a nonconverging dual infeasibility, indicating a lack of optimality [55]. In this study, it is thus chosen to cast the multi-objective optimization problem as a single

[§§]The IPOPT optimization iteration history for the high-speed PTCB trajectory at $V_{TO} = 128.6$ m/s (250 kts) is shown in Appendix B.

objective optimization problem with the flyover noise level as an objective function and an upper bound constraint on the lateral noise level:

$$\tau^*(t), k^*_{\text{rot}} = \underset{\substack{TS\in(0,1]\\ k_{\text{rot}}\in[1.1,1.5]}}{\text{argmin}} \quad EPNL_{\text{flyover}}$$
$$\text{subject to} \quad EPNL_{\text{lateral}} < EPNL_{\text{lateral,upper bound}}$$
$$\text{boundary and path constraints (Table 2)} \tag{5}$$

The value for the upper bound of lateral *EPNL* in Eq. (5) is informed by the trajectory operational space, as will be explained in Sec. V. One could also choose to minimize the lateral noise by using the STCB operational space to find an informed estimate of the minimum achievable flyover noise. To assess whether the solution of the optimal control problem in Eq. (5) is a global minimum, one can perform a sensitivity analysis for various lateral upper bound constraints, which is beyond the scope of this work.

2. *Nondifferentiable Definition of the Lateral Certification Noise Metric*

The lateral certification noise level is defined as the maximum level measured by any microphone on the sideline at $y = 450$ m. ICAO Annex 16 Volume I §3.3.2.2 requires measurement points within 10 m on the lateral sideline [12]. In this work, this requirement is relaxed to limit the computational cost. The maximum sideline *EPNL* is approximated using a series of N discrete sideline observers. The lateral *EPNL* is thus defined as

$$EPNL_{\text{lateral}} = \max_{j\in[1,N]} EPNL_{\text{sideline},j} \tag{6}$$

The position of the sideline observers is chosen such that the maximum noise level along the sideline occurs within the interval. The maximum function in Eq. (6) is not continuously differentiable and thus cannot be used in gradient-based optimization. Equation (6) is therefore approximated using the Kreisselmeier and Steinhauser log-sum-exp (LSE) function [56]:

$$\max_{j\in[1,N]} EPNL_{\text{sideline},j} \approx a + \frac{1}{k}\log\sum_{j=1}^{N}\exp[k(EPNL_{\text{sideline},j} - a)] \tag{7}$$

The constant a is used to avoid overflow of the smooth maximum approximation and is set equal to the maximum sideline noise level, i.e., $a = \max_{j\in[1,N]} EPNL_{\text{sideline},j}$ [56]. Finally, a smoothing factor $k = 50$ is used. Equation (7) is substituted in the upper bound constraint of Eq. (5). A reasonable value for the smoothing factor k is determined using a sample problem by considering the trade between the smoothness of the approximation in Eq. (7) and the ability to reach the maximum.

3. *Region of Undetermined Control for Conventional Certification Noise Metrics*

The conventional *EPNL* certification noise metric as prescribed by ICAO Annex 16 Volume I [12] is defined in its integral form by

$$EPNL = 10\log_{10}\left[\frac{1}{\Delta t}\int_{t_1}^{t_2} 10^{0.1PNLT(t)}\,\mathrm{d}t\right] \tag{8}$$

A reference duration $\Delta t = 10$ s is used in Eq. (8). The times (t_1, t_2) are determined by the times for which $PNLT > (\max(PNLT) - 10$ TPNdB) [12]. The domain of influence of a control variable at time step t_{control} is $t > t_{\text{control}}$ (Fig. 5a). The domain of influence of *EPNL* is thus $t \in [t_1, t_2]$ (Fig. 5b). Comparing the domain of dependence of *EPNL* to the domain of influence of the trajectory control, a region of undetermined control is obtained for $t > t_2$, since control variables for $t > t_2$ are not influencing the optimal control objective function. This region is illustrated by the hatched region in Fig. 5.

This region of undetermined control is avoided by defining a modified acoustic objective function, i.e., the *integrated tone-corrected perceived noise level* (*IPNLT*):

$$IPNLT = 10\log_{10}\left[\frac{1}{\Delta t}\int_{0}^{\infty} 10^{0.1PNLT(t)}\,\mathrm{d}t\right] \tag{9}$$

The integrals of the antilog of *PNLT* in Eqs. (8) and (9) are plotted in Fig. 6. The upper limit of the integral in Eq. (9) is approximated as the final time step of the trajectory, i.e., t_{end} at which $x = x_{\text{end}}$ (see Table 3). The tails of the antilog of *PNLT*—outside the *EPNL* domain of dependence—are by definition at least one order of magnitude smaller than the peak. Thus, *IPNLT* is a suitable modified objective function for the optimal control problem defined in Eq. (5).

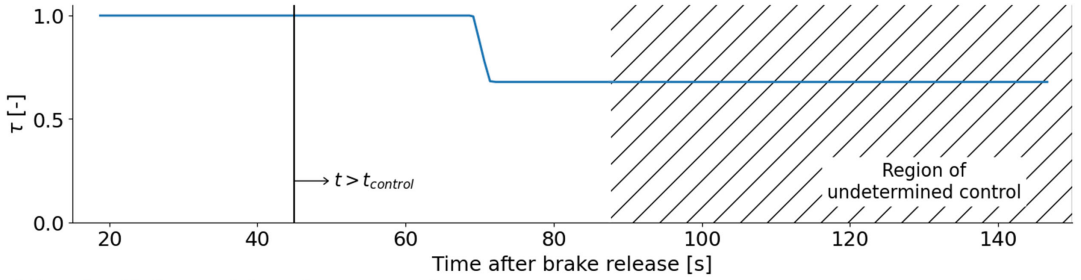

a) Domain of influence of the trajectory control, $t > t_{control}$

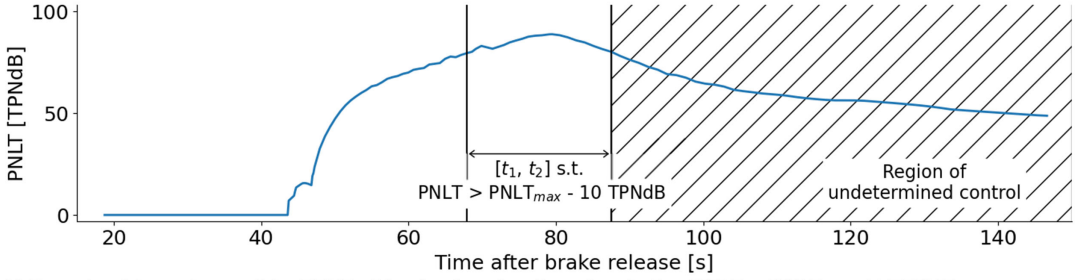

b) Domain of dependence of the EPNL objective function, $[t_1, t_2]$ such that PNLT > $PNLT_{max}$-10 TPNdB

Fig. 5 Illustration of the region of undetermined control for NASA STCA Standard trajectory [7,29] at the flyover microphone using *EPNL* as objective function.

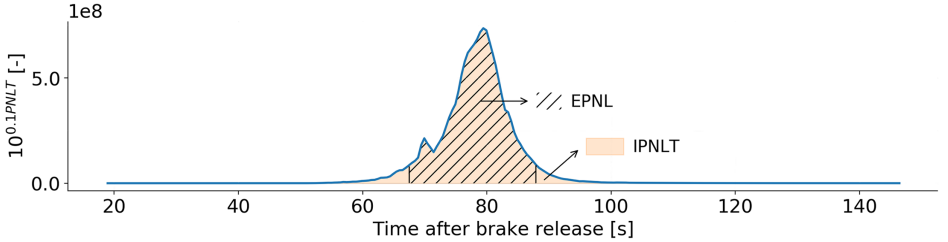

Fig. 6 Illustration of *EPNL* and the *IPNLT* metrics for the NASA STCA Standard trajectory [7,29] at the flyover microphone; $\Delta = IPNLT - EPNL = 0.32$ dB.

4. Weak Minima for Integral Objective Functions

The *EPNL* and *IPNLT* noise metrics are integral objective functions that can be discretely represented as a multi-objective optimization:

$$\text{objective} = \int_{t_1}^{t_2} y(t)\,\mathrm{d}t \approx \sum_{t_i \in [t_1, t_2]} y_i \Delta t \tag{10}$$

Similar to Sec. IV.B.1, the sum in the objective in Eq. (10) leads to a multi-objective optimization problem prone to weak minima within the constraints of the problem, corresponding to oscillatory solutions. This results in a lack of dual-infeasibility convergence in the IPOPT optimization algorithm. The convergence criterion for the optimization algorithm is altered to the convergence of the primal infeasibility only, i.e., $i_{\text{pr}} < 1 \cdot 10^{-4}$. This forces the optimization algorithm to arrive at a trajectory and associated control time history without constraint violation, despite having no proof of optimality through dual infeasibility convergence. An example of the IPOPT convergence history for the PTCB trajectory at $V_{TO} = 250$ kts is shown in Appendix B. Furthermore, the number of number segments, n_{seg}, and transcription order n_{order} of the Gauss–Lobatto transcription must be carefully selected when using integral objective functions in trajectory optimization. Too many segments can result in oscillatory behavior in the control time series, whereas too few will not be able to capture higher order trends. The PTCB control schedules in this paper use $n_{\text{seg}} = 8$ and $n_{\text{order}} = 3$.

V. Results and Discussion

A. Certification Noise Levels of STCB Operational Space for NASA STCA

Figure 7 shows the lateral, flyover, and takeoff *EPNL* for the STCB trajectory operational space of the NASA STCA at both the low and high takeoff speeds. The operational space is determined by 2 degrees of freedom, namely (z_{cb}, τ_{cb}).

The STCB operational space exhibits an inherent tradeoff between lateral and flyover *EPNL* at both takeoff speeds. A high-altitude thrust cut-back near the domain of dependence of the flyover microphone enables the aircraft to a) climb as high as possible above the flyover microphone, and b) reduce its source noise contribution at the flyover microphone using the thrust cut-back. However, the lateral microphone then measures the source noise from engines at full thrust, resulting in high lateral noise. Alternatively, a low-altitude thrust cut-back, before reaching the domain of dependence of the lateral microphone, enables the aircraft to reduce its local lateral source noise contribution at the cost of having a lower altitude above the flyover microphone, thereby increasing flyover noise. Figure 7 clearly shows the altitude above which cut-backs do not have any effect on the lateral noise ($z_{cb} > 300$ m). This *inherent tradeoff* between lateral and flyover noise levels is highlighted by the two distinct local minima in the contour plot of the takeoff *EPNL*. The control variables corresponding to the local minima in the contour plots of Fig. 7 are marked with an asterisk (*).

Similar to the low-speed trajectories, the high-speed operational space is characterized by two local minima, governed by the trade in lateral and flyover noise levels. The minimum cut-back thrust setting reduces from $\tau_{\min}|_{V_2+20\text{ kts}} = 0.75$ at low takeoff speeds to $\tau_{\min}|_{250\text{ kts}} = 0.4$ at high takeoff speeds. This is driven by the improved aerodynamic efficiency during takeoff, i.e., $L/D|_{250\text{ kts}} = 13.1$, compared to $L/D|_{V_2+20\text{ kts}} = 8.3$. As the noise signature of the NASA STCA is dominated by the jet-mixing noise contribution, an increased flight velocity also enables reduced source noise because of the reduction in shear of the jet, represented by $(V_j - V_0)$. Furthermore, at higher takeoff speeds, the duration correction of the *EPNL* noise metric reduces, resulting in lower certification noise levels.[¶]

The operational space of the STCB trajectory in Fig. 7 includes two local minima of takeoff *EPNL* for each takeoff speed:

1) *Standard trajectory (S)*: The high-altitude cut-back ($z \geq 260$ m) takeoff trajectories at low takeoff speed ($V_{TO} = V_2 + 20$ kts) are currently abiding by the ICAO Annex 16 Volume I noise certification procedures for subsonic aircraft. The minimum takeoff noise level for such trajectory in the (z_{cb}, τ_{cb}) operational space is equal to $EPNL_{\text{TO}} = 188.2$ EPNdB.

2) *Advanced trajectory* (A_1): Reduced cut-backs altitudes ($z_{cb} < 260$ m) enable up to 3.0 EPNdB takeoff certification noise reduction.

3) *Advanced trajectory* (A_2): Increased takeoff velocities ($V_{TO} = 250$ kts) at $z \geq 260$ m enable up to 4.1 EPNdB takeoff certification noise reduction.

4) *Advanced trajectory* (A_3): A combination of both reduced cut-back altitude and increased takeoff velocity enables up to 7.0 EPNdB takeoff certification noise reduction.

The certification noise levels of these STCB trajectories are summarized in Fig. 10 in Sec. V.D.

B. Sideline Noise Characteristics of Single-Thrust Cut-Back Trajectories

Figure 8 shows the sideline noise levels for the two local minima in the STCB takeoff trajectory operational space of the NASA STCA at $V_2 + 20$ kts takeoff speed: the high-altitude ($z_{cb} = 750$ m, $\tau_{cb} = 0.75$) and low-altitude ($z_{cb} = 25$ m, $\tau_{cb} = 0.75$) trajectories. Sideline noise levels for $x < 1$ km are not considered to avoid an (invalid) 10 dB down region on only the right side of $PNLT_{\max}$. Three characteristic regions are identified along the sideline:

1) *Aircraft ground roll:*

During the ground roll, the aircraft has the same propagation distance to all microphones on the sideline. These noise measurements of these microphones are only shifted in time. As the aircraft accelerates along the runway after brake release, the jet mixing source noise reduces as the shear between the jet and ambient reduces, which results in reduced sideline noise. Further, ground effects as well as lateral attenuation effects are dominant in this region. Note that this region (before the liftoff point) is not taken into account when computing the maximum sideline noise.

2) *Aircraft liftoff:*

Shortly after liftoff, the ground effects and lateral attenuation effects on the propagated noise reduce as the microphone elevation angle increases, resulting in increased sideline noise. The slope of the sideline noise in this region is dependent on the rate of climb along the takeoff trajectory.

[¶]The effective perceived noise level is defined as $EPNL = \max(PNLT) + D$, where the duration correction is given by $D = 10\log_{10}[(1/T)\int_{t_1}^{t_2} \text{antilog}(PNLT/10)\,\mathrm{d}t] - \max(PNLT)$; t_1 and t_2 are the times for which PNLT is above $\max(PNLT) - 10$TPNdB; and $T = 10$ s is a normalizing time constant. At higher speeds, $\Delta t = t_2 - t_1$ decreases, resulting in a decreased duration correction.

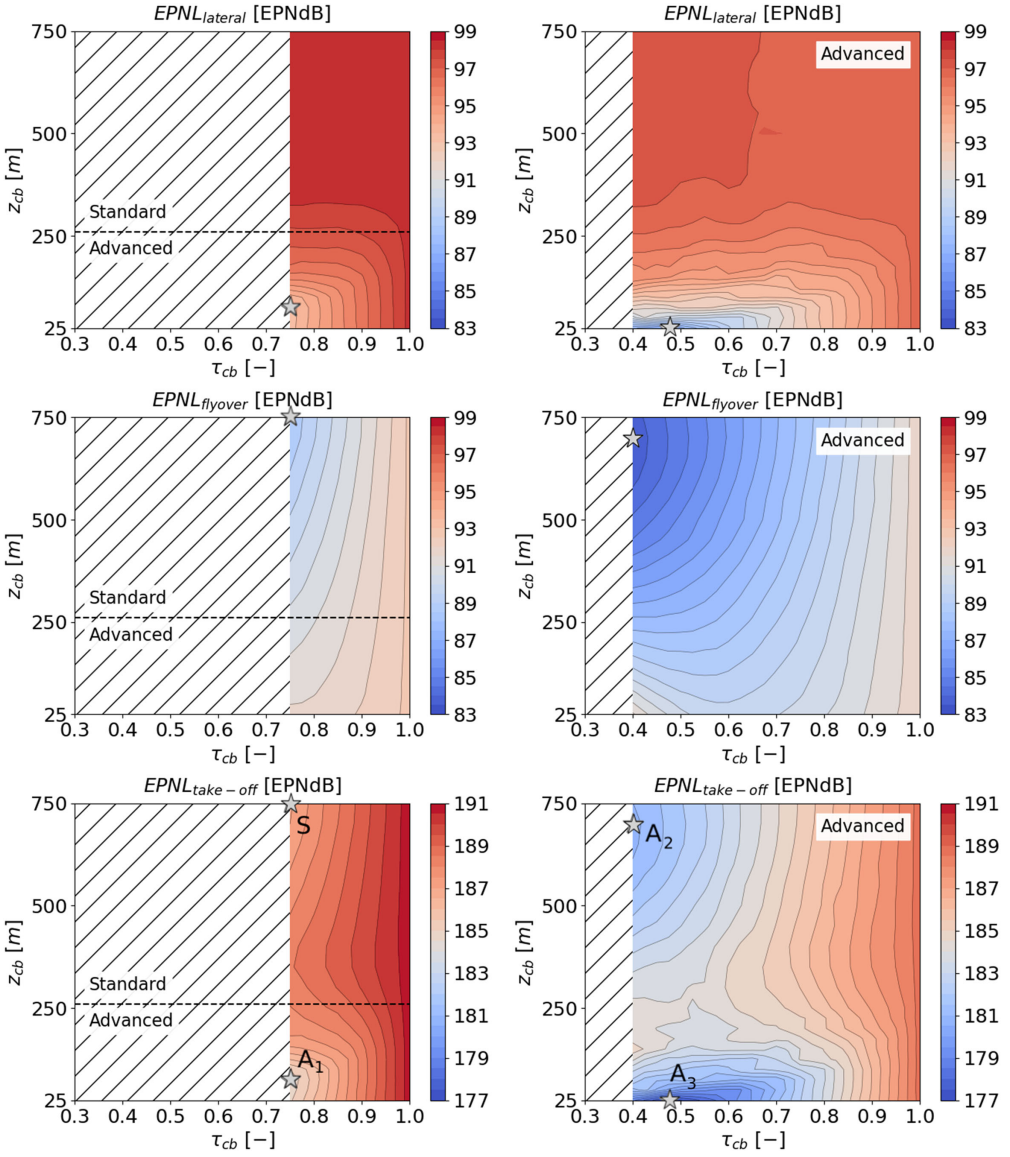

Fig. 7 Lateral (top), flyover (middle), and takeoff (bottom) *EPNL* for the STCB operational space for the NASA STCA. Control parameters of local minima are indicated by an asterisk (*); hatched area does not satisfy steady-level flight at OEI.

3) *Aircraft climb-out:*

As the aircraft climbs out further, the distance between the aircraft and the microphones increases further, causing the sideline noise to decrease. Similar to the liftoff region, the slope of the sideline noise is dependent on the rate of climb along the takeoff trajectory.

Figure 8 shows that the low-altitude single thrust cut-back occurs before the sideline noise peak and thus has an impact on the lateral noise levels. The high-altitude thrust cut-back occurs after the sideline noise peak and thus only impacts the flyover microphone noise level. The three distinct regions are also observed for the

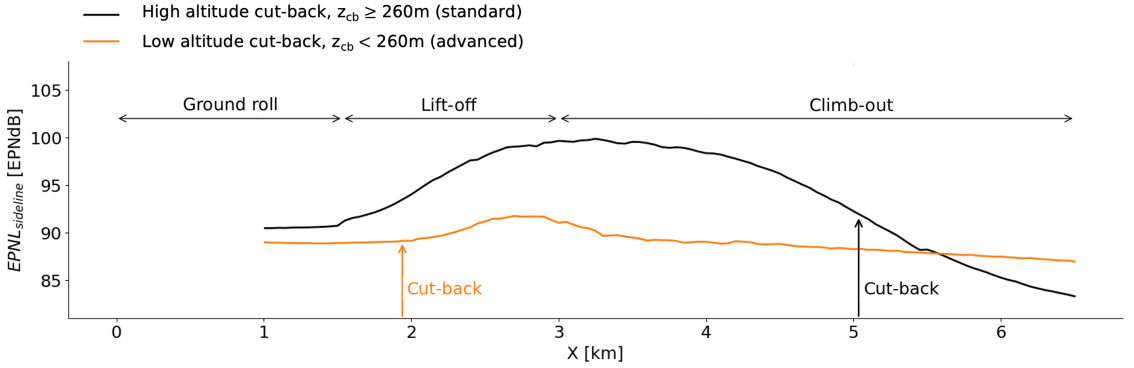

Fig. 8 Sideline noise levels for the best high-altitude ($z_{cb} = 750$ m, $\tau_{cb} = 0.75$) and low-altitude ($z_{cb} = 25$ m, $\tau_{cb} = 0.75$) single thrust cut-back takeoff trajectory of the NASA STCA at $V_2 + 20$ kts.

takeoff trajectories of the NASA STCA at high-speed takeoff. The sideline noise characteristics are critical in determining noise-optimal takeoff trajectories using PTCB control strategies, as presented in Sec. V.C.

C. Effect of PTCB on Takeoff Noise Levels

It is hypothesized that PTCB trajectories can enable takeoff noise reduction because of their increased degrees of freedom compared to STCB trajectories and, thus, eliminate the trade between lateral and flyover noise established in Sec. V.A.

As introduced in Sec. IV.B.2, the lateral noise for the PTCB trajectories is approximated using a series of N sideline observers. The following sideline observer interval is chosen:

$$x \in [x_{\text{obs},1} = 1000, x_{\text{obs},N=16} = 6250]\ \text{m} \rightarrow \Delta x_{\text{obs}} = 350\ \text{m} \quad (11)$$

The choice of sideline observer is informed by the sideline noise characteristics, as outlined in Sec. V.B. The interval of sideline observers needs to capture the liftoff and climb-out regions (see Fig. 8), i.e., the location of the maximum sideline noise. The start of the interval is adapted to reflect the change in their takeoff distance. The lateral $EPNL$ upper limit in Eq. (5) is set to the minimum lateral $EPNL$ from the STCB operational space in Fig. 7, i.e., 93.2 EPNdB for $V_{\text{TO}} = 197$ kts and 86.9 EPNdB for $V_{\text{TO}} = 250$ kts. The flight path (x, z), velocity V, thrust-setting schedule τ, and sideline $EPNL$ for the PTCB trajectories of the NASA STCA are shown in Fig. 9 and compared to the low- and high-altitude STCB trajectories from Sec. V.A. The PTCB trajectories are computed for both takeoff speeds.

The PTCB thrust-setting schedules for both velocity constraints are characterized by a thrust reduction followed by a *thrust bump*. At any point along the takeoff trajectory—by balancing the source noise and propagation noise—the optimal control framework applies as much thrust as possible to climb as high as possible above the flyover microphone. It is noted that this continuous thrust control schedule needs to be implemented in the engine FADEC rather than executed by the pilot. Additionally, while the optimal thrust bump procedure enables noise reduction for the STCA, such a continuously variable throttle control is more complex to program in day-to-day operations compared to simpler thrust cut-backs with steadily decreasing thrust.

The resulting sideline ($y = 450$ m) $EPNL$ for the PTCB trajectories is characterized by a *noise plateau*, as opposed to the distinct noise peak for the STCB trajectories. As the lateral noise level is governed by the maximum on the sideline, the STCB trajectories do not use the full potential to climb above the flyover microphone when generating such a noise peak. The shaded area between the sideline noise level for the low-altitude STCB and the PTCB takeoff trajectories in Fig. 9 is a proxy for the benefit of the PTCB trajectory. The sideline noise of the low-altitude STCB trajectory at $V_{TO} = V_2 +$ 20 kts already exhibits a relatively flat maximum and thus benefits negligibly from the automatic continuous thrust control. The PTCB

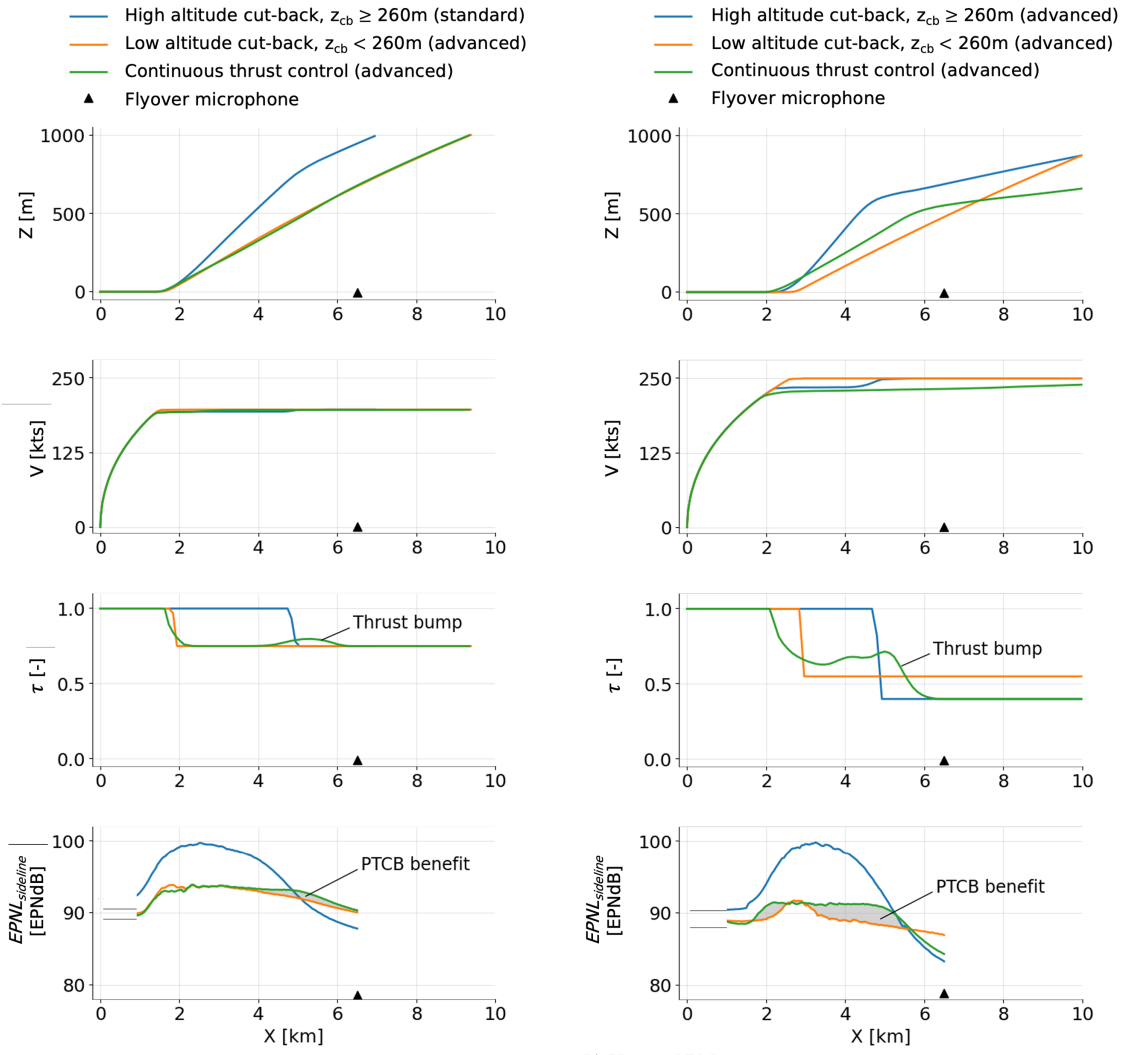

Fig. 9 Comparison of the flight path (top), velocity (top middle), thrust setting (bottom middle), and sideline $EPNL$ (bottom) between the high- and low-altitude STCB, and PTCB trajectories of the NASA STCA.

benefit at $V_{TO} = 250$ kts is thus larger, as shown in Fig. 9. By enabling such automatic continuous thrust control along the takeoff trajectory, the takeoff noise level is reduced by an additional 3.6 EPNdB compared to the best STCB trajectory, i.e., the low-altitude high-speed STCB. The certification noise level of both PTCB trajectories is summarized in Fig. 10 in Sec. V.D.

Finally, it is of interest to assess the rate of change of engine thrust setting throughout the PTCB trajectory, i.e., $d\tau(t)/dt$. The rate of change of engine thrust setting is between -9.3 and $+1.5\%/s$ throughout the trajectory. These bounds set a design requirement on the engine components for future low-noise propulsion systems for SST. It is assumed that these rates are achievable with CFM56-based engine technology levels used in the NASA STCA propulsion system.

D. Comparison of Takeoff Trajectory Certification Noise Levels to ICAO Stringency Levels

The lateral, flyover, and cumulative *EPNL* of the STCB and PTCB trajectories in Secs. V.A and V.C are compared to the current ICAO Annex 16 Volume I Chapter 14 noise limits in Fig. 10. This reference is chosen since the United States has recently declared their support for the development of supersonic LTO noise standards based on Chapter 14 limits for commercial subsonic transport [57]. The ICAO Annex 16 Volume I Chapters 3 and 4 cumulative noise limits are also shown in Fig. 10 for reference. The approach noise for the NASA STCA is constant and equal to 98.6 EPNdB.

Figure 10 shows that advanced takeoff trajectories enable 10.6 EPNdB cumulative noise reduction for the NASA STCA, compared to a standard takeoff trajectory abiding by the subsonic noise certification standards in ICAO Annex 16 Volume I: 7.0 EPNdB by reducing the allowable control altitude and increasing the takeoff speed and 3.6 EPNdB by using automatic continuous thrust control. The advanced takeoff trajectories are required for the NASA STCA to meet the ICAO Annex 16 Volume I Chapter 4 noise limits. However, the cumulative noise level still exceeds the Chapter 14 noise limits by 5.1 EPNdB. The increase in takeoff velocity from $V_2 + 20$ kts to 250 kts is found to be the most effective measure to reduce SST takeoff noise levels as this reduces the jet shear and associated jet mixing noise. Even higher takeoff velocities above 250 kts could enable more noise reduction by further decreasing the jet shear. Those could be achieved by an in-air acceleration segment combined with an automatic flap retraction procedure. However, procedures using PHLDs are beyond the scope of this paper and left for future research.

The assessment of advanced takeoff trajectories for takeoff noise reduction in this paper is applied to the NASA STCA. It is thus of interest to compare the noise level of the advanced trajectory with the lowest cumulative noise level (-5.1 EPNdB cumulative margin to ICAO Annex 16 Chapter 14) with the result obtained by Berton [18] (-1 EPNdB cumulative margin). The differences in results are attributed to the use of a) an in-air acceleration segment, b) PHLDs, and c) a different method for computing lateral *EPNL* in the presence of ground effects in Berton [18]. Section V.E further elaborates on the uncertainty of the quantitative results presented in this paper.

E. Uncertainty Assessment

The aircraft noise prediction methods (see Table 4) used in this work have been originally developed for (conventional) subsonic transport aircraft. The following uncertainties are present in the semi-empirical source noise estimation methods:

1) *Fan broadband noise and tones:* Propulsion systems for SST are likely to use two-stage fan designs to produce the high fan pressure ratios ($\pi_{\text{fan}} \sim 2$) required for supersonic cruise. Additionally, they are likely to employ auxiliary inlet doors to allow for increased airflow to meet takeoff thrust requirements. Since the Heidman method [40] implementation is developed for engines with single-stage fans without auxiliary inlet doors, the noise generated by these components is not accounted for in pyNA. Bridges [58] uses wind tunnel data from two-stage fans developed under the NASA High Speed Civil Transport (HSCT) program to estimate the impact of multistage fans on fan noise for SST. In this work, it is reasoned that SST engines have significantly longer inlets relative to engines for subsonic transport. Thus, even though uncertainties exist in the fan noise prediction methods, their effect on the overall aircraft noise levels can be limited through the use of additional acoustic liner treatment along the inlet walls.

2) *Jet mixing noise:* Henderson et al. [59] performed an acoustic flight test of a jet mixing noise dominant subsonic Learjet 25 aircraft to assess the SAE ARP-876 jet mixing noise estimation. They found that the SAE ARP-876 method underestimates the jet mixing noise by 2.5–3.5 EPNdB. Furthermore, propulsion systems for SST are likely to use internal mixers to combine core and bypass ducts as well as external plugs to minimize boat-tail drag. Such plugs and mixers are not accounted for in the SAE ARP-876 [45] method for single stream jet mixing noise. Bridges et al. [58] quantified that the uncertainty on jet mixing noise for SST propulsion systems is up to 3.85 EPNdB for the NASA STCA when using the SAE ARP-876 model. Furthermore, Bridges [60] assessed the excess noise generated in engines using internal mixers with external plug exhaust systems.

3) *Airframe noise:* The Fink method [46] for airframe source noise was developed for conventional subsonic transport [47]. The high-speed research (HSR) correction factor [47] is obtained from a low-speed aeroacoustics wind tunnel test of a 3% double delta wing SST scale model. A physics-based model for the airframe noise of SST configurations has not been developed. However, since the jet mixing noise is dominant during takeoff of SST, the impact of airframe noise uncertainty is expected to be small.

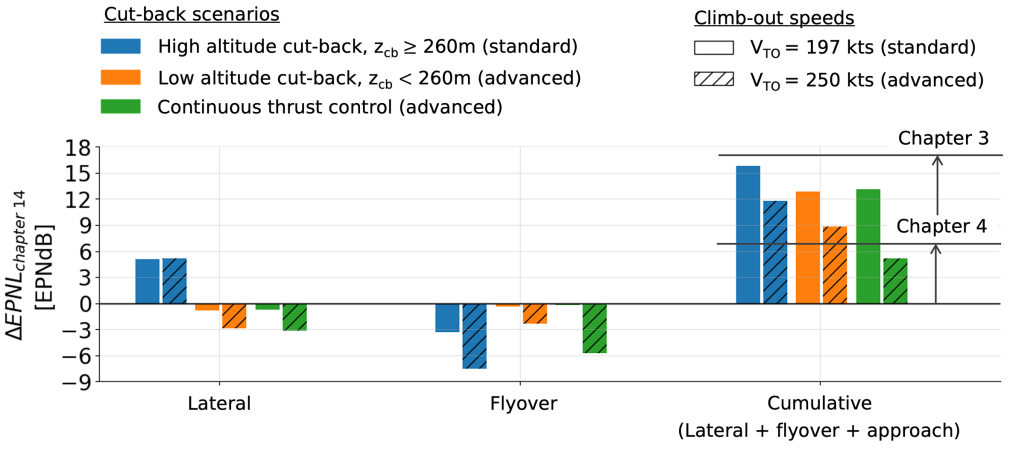

Fig. 10 Comparison of the lateral, flyover, and cumulative certification noise levels of standard and advanced takeoff trajectories with the ICAO Annex 16 Volume I Chapter 14 noise limits [12].

The following uncertainties are present in the semi-empirical noise propagation methods:

1) *Engine noise shielding by the airframe* has not been accounted for in the noise assessments. The wide variety of possible SST vehicle configurations causes uncertainty for noise shielding. The noise levels for aircraft with under-wing-mounted engines are not affected by shielding effects. For aircraft with fuselage-mounted engines, the forward radiated noise is reduced by wing planform shielding. The noise from fuselage-mounted engines has jet-by-jet shielding for lateral microphones, which is accounted for via an engine installation term in the SAE AIR-5662 method [50].

2) *Lateral attenuation effects*, as described by SAE AIR-5662 [50], are a post hoc subtraction from the aircraft certification noise levels. The post hoc subtraction of the lateral attenuation correction is applied to the certification noise levels and thus is not dependent on one-third octave band frequency. A physics-based lateral attenuation model is lacking, and thus the effects are determined empirically. The uncertainty in the SAE AIR-5662 method is a result of the large scatter exhibited in the empirical data [50]. Additionally, *ground reflection propagation effects* are described using an analytical model, whereas lateral attenuation effects are described using an empirical model. The combined use of both methods introduces a double bookkeeping error, as the empirical lateral attenuation model includes the influence of ground reflections implicitly. As shown in Fig. 8, the ground reflection and lateral attenuation effects are driving the shape of the sideline noise. The uncertainty in these propagation effects is thus expected to have the largest impact on the PTCB control schedules and their corresponding noise reduction potential. To reduce this uncertainty, Berton [61] proposes a method to use ground reflection and lateral attenuation noise models simultaneously. Furthermore, ICAO has considered the idea of using ground-based microphones rather than pole-mounted microphones at 1.2 m [62–64]. The use of such microphones would simplify the interaction of ground reflection and lateral attenuation effects. However, a mathematical transformation to allow compatibility with and comparisons to legacy pole-mounted measurements has not been developed yet, which has prevented their implementation with the noise certification framework.

VI. Conclusions

No previous work has considered the design and optimization of advanced takeoff trajectories for SST using *automatic continuous control schedules of engine thrust* to minimize takeoff noise levels. This research gap is addressed in this paper by identifying the attributes and quantifying the potential of advanced takeoff trajectories designed for noise reduction. The following are shown:

1) Capitalizing on excess engine thrust and improved aerodynamic efficiency at higher takeoff speeds, i) automatic continuous control of thrust, ii) increased takeoff speed, and iii) reduced cut-back altitude compared to conventional trajectories currently used for subsonic transport, can reduce the cumulative certification noise level by 10.6 EPNdB for a Mach 1.4 business jet. The key enabler for community noise reduction is the increased takeoff speed.

2) This cumulative certification noise reduction is insufficient to meet current subsonic transport noise limits without additional VNRS procedures, noise reduction technologies, engine cycle redesigns, or modified airplane architectures not considered in this paper.

3) Effective PTCB control schedules for takeoff noise minimization are characterized by a thrust cut-back followed by a newly discovered thrust bump. Such a thrust control schedule yields a noise plateau on the lateral sideline rather than a distinct peak observed for standard takeoff trajectories.

The following areas for further research are suggested:

1) Assess the potential of operational part-power takeoff procedures [7,16] in combination with the advanced takeoff trajectories assessed in this paper.

2) Reduce the uncertainty in the quantitative results by improving the understanding and numerical modeling of the lateral attenuation effects as well as their interaction with the ground reflection and attenuation effects.

3) Assess the impact of the advanced trajectories proposed in this paper on the community noise exposure around airports; possible community noise metrics are the (local) single event sound exposure level and the (integrated) noise footprint contour area. Furthermore, it is recommended to assess *airport-dependent* advanced takeoff and approach trajectories to minimize community noise exposure. Increasing the takeoff trajectory degrees of freedom can enable noise reductions in highly populated areas around the airport, e.g., including varying bank angles. The noise-optimal control framework developed in this paper can be applied to develop such trajectories. Instead of selecting the sideline and flyover certification microphones in the objective function, microphones can be placed in highly populated areas around airports to optimize the three-dimensional flight path for community noise exposure. Furthermore, flying over waterways is an additional measure for aircraft-dependent LTO procedures for noise reduction.

4) Carry out flight tests of the advanced takeoff trajectories for SST noise reduction. This would enable the assessment of the (computational) results presented in this thesis using experimental data.

5) Assess how the quantitative results in this paper scale for a broad range of SST (e.g., with different cruise Mach numbers and aircraft sizes).

Appendix A: Governing Equations and Verification of Trajectory Module

A. Governing Equations

1. Atmospheric Module

The 1976 US Standard Atmospheric (USSA) model [65], given by Eq. (A1), is used to compute atmospheric properties. The model computes the ambient temperature T_0, pressure p_0, density ρ_0, speed of sound c_0, dynamic viscosity μ_0, and characteristic acoustic impedance $I_0 = \rho_0 c_0$, at altitude z given the sea level atmospheric conditions (referenced by subscript "sl"). A temperature deviation from the USSA model is implemented using ΔT_{USSA}. In Eq. (A1), the ratio of specific heats, the gravitational constant, the air gas constant, and the atmospheric lapse rate are denoted by γ, g, R, and λ, respectively.

$$
\begin{aligned}
T_{\text{USSA}} &= T_{sl} - \lambda z & \rho_0 &= \frac{p_0}{RT_0} \\
T_0 &= T_{sl} - \lambda z + \Delta T_{\text{USSA}} & c_0 &= \sqrt{\gamma R T_0} \\
p_0 &= p_{sl}\left(\frac{T_{\text{USSA}}}{T_{sl}}\right)^{g/\lambda R} & \mu_0 &= \mu_{sl}\frac{\left(1.38313\left[\frac{T_0}{T_{sl}}\right]^{1.5}\right)}{\left(\frac{T_0}{T_{sl}} + 0.38313\right)}
\end{aligned}
\tag{A1}
$$

2. Aerodynamics and CL-CD Modules

The aircraft aerodynamic lift coefficient C_L and drag coefficient C_D are computed from a look-up table as a function of the wing angle of attack α and the flap deflection angles θ_{flap}. The aircraft landing gear is retracted upon clearing the obstacle height. A constant drag component $C_{D,lg}$ is added to the aerodynamic drag coefficient when the landing gear is extended, as defined by the parameter I_{lg}:

$$
I_{lg} = \begin{cases} 1 & \text{for ground roll, rotation, and liftoff phases} \\ 0 & \text{for automatic and continuous thrust, and cut-back phases} \end{cases}
\tag{A2}
$$

The aircraft lift and drag forces are computed as follows:

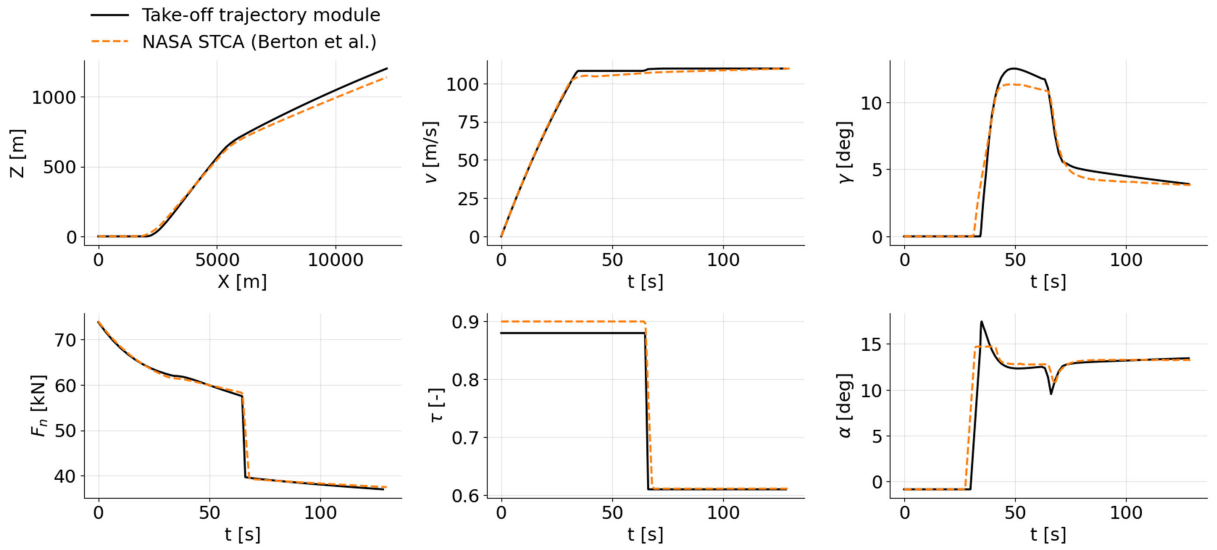

Fig. A1 Verification of the trajectory module against the NASA STCA Standard trajectory [7,29]: flight path parameters x, z, v, and γ (top) and trajectory control parameters F_n, τ, and α (bottom).

$$L = C_L(\alpha, \theta_{\text{flap}})\frac{1}{2}\rho_0 V^2 S$$
$$D = [C_D(\alpha, \theta_{\text{flap}}) + I_{lg} \cdot C_{D,lg}]\frac{1}{2}\rho_0 V^2 S \tag{A3}$$

3. Propulsion Module

The engine thermodynamic cycle deck is developed for a CFM56-5B3 based derivative engine for the NASA STCA using the numerical propulsion system simulation (NPSS) software [32]. A look-up table is implemented of the engine parameters as a function of flight Mach number $M_0 \in [0, 0.5]$, flight altitude $z \in [0, 5000]$ m, and engine thrust setting $\tau \in [0.3, 1.05]$. In addition to computing the net thrust F_n, the propulsion module computes engine operational variables necessary to determine the engine noise source strength (see Sec. III.C). More details on the development of the engine cycle deck can be found in Prashanth et al. [34].

4. Flight Dynamics Module

A set of two-dimensional flight dynamics equations is used in the trajectory module, describing the horizontal and vertical motion (x, z) of the aircraft as a function of time t. The rate equations for the position vector (x, z) are given by

$$\dot{x} = V\cos\gamma \qquad \dot{z} = V\sin\gamma \tag{A4}$$

The rate equations for velocity V are given by

$$\dot{V} = \begin{cases} \frac{1}{m}(F_n\cos\tilde{\alpha} - D - F_{\text{fric}} - mg\sin\gamma) & \text{for ground roll and rotation phases} \\ \frac{1}{m}(F_n\cos\tilde{\alpha} - D - mg\sin\gamma) & \text{for liftoff, automatic and continuous thrust, and cut-back phases} \end{cases} \tag{A5}$$

In Eq. (A5), the rolling friction force is given by: $F_{\text{fric}} = \mu(mg - L)$, where mg is the aircraft weight. The effective angle of attack $\tilde{\alpha}$ is given by the sum of the wing angle of attack α, the thrust inclination angle i_{F_n}, and the wing installation angle α_0, i.e., $\tilde{\alpha} = \alpha + i_{F_n} - \alpha_0$. The rate equations for the climb angle γ are given by

$$\dot{\gamma} = \begin{cases} 0 & \text{for ground roll and rotation phases} \\ \frac{1}{mV}(F_n\sin\tilde{\alpha} + L - mg\cos\gamma) & \text{for liftoff, automatic and continuous thrust, and cut-back phases} \end{cases} \tag{A6}$$

As given in Table 3, the rate of change of the angle of attack, $(d\alpha/dt) =$ constant, is explicitly prescribed in the rotation phase and equal to 3.5 deg/s. The end of the rotation phase is determined when the aircraft load factor, $n = (F_n\sin\tilde{\alpha} + L/mg\cos\gamma) = 1$.

B. Verification

The takeoff trajectory module is verified against the NASA STCA Standard takeoff trajectory [7,29], computed using the NASA FLight Optimization System (FLOPS) software [36]. The comparison of the flight path variables (x, z, α, γ, v) and engine parameters (τ, F_n) between the trajectory computed using the takeoff model and the NASA STCA Standard trajectory is shown in Fig. A1.

It can be seen that the trajectory module is able to closely compute the flight path variables of the NASA Standard trajectory. In this verification—as the engine model used in this paper differs from the NASA STCA engine model developed by Berton [29]—the engine thrust setting is chosen to match the engine net thrust profile of the NASA STCA Standard takeoff trajectory. Small differences in the angle of attack control parameter are expected due to differences in control logic between Dymos and NASA FLOPS.

Appendix B: Weak Minima as a Result of Integral Objective Functions

Figure B1 shows the objective function *EPNL* at the takeoff certification microphones as a function of the iteration number for the high-speed PTCB trajectory at $V_{\text{TO}} = 128.6$ m/s (250 kts). Furthermore, the control variables (rotation speed ratio k_{rot}, angle of attack α, and thrust setting τ) are shown as a function of the optimization iteration number. For the continuous controls (α and τ), Fig. B1 shows both the discretized control vector elements (i.e., α_i and τ_i, with index i) as well as the comparison of the continuous control vector between the final iteration and the average over all iterations.

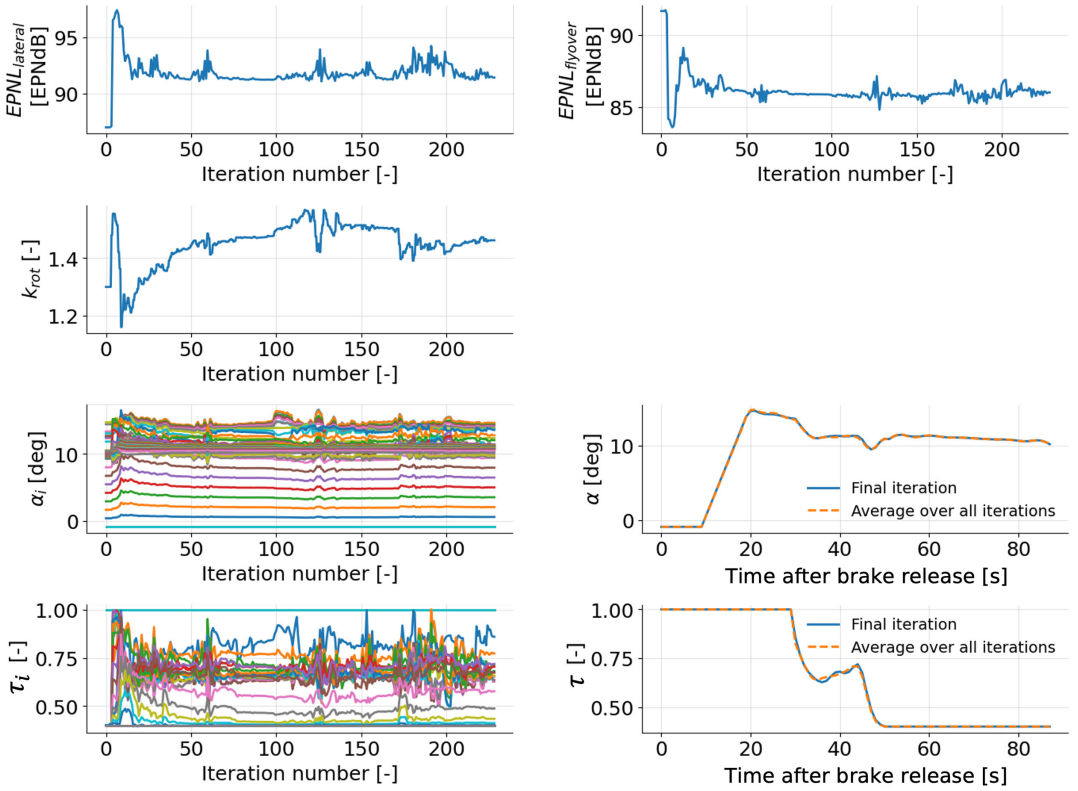

Fig. B1 IPOPT optimization history for PTCB trajectory at $V_{max} = 128.6$ m/s (250 kts): objective function (top row), rotation speed ratio k_{rot} (second row), angle of attack α (third row), and thrust setting τ (bottom row).

Acknowledgments

This research was funded by the U.S. Federal Aviation Administration (FAA) Office of Environment and Energy through ASCENT, the FAA Center of Excellence for Alternative Jet Fuels and the Environment, project 47 through FAA Award Number 13-C-AJFE-MIT under the supervision of László Windhoffer and Ralph Iovinelli. Any opinions, findings, conclusions, or recommendations expressed in this material are those of the authors and do not necessarily reflect the views of the FAA. The authors would like to acknowledge Jeff Berton and Dennis Huff from the NASA Glenn Research Center, and Muni Majigi from the FAA for their advice on aircraft acoustics and noise certification. The authors would also like to thank Justin Gray and Daniel Ingraham from the NASA Glenn Research Center for their valuable guidance on optimization and working with the OpenMDAO and Dymos software.

References

[1] Tanner, C. S., "Noise Measurement of Concorde 02 Approach and Takeoff at Dallas Ft. Worth and Dulles International Airports," U.S. Environmental Protection Agency TR EPA 550/9-74-013, 1974, https://nepis.epa.gov/Exe/ZyPDF.cgi/9101VL7E.PDF?Dockey=9101VL7E.pdf [retrieved 11 May 2022].

[2] Hay, J. A., "Concorde–Community Noise," Soc. of Automotive Engineers 760898, 1976. https://doi.org/10.4271/760898

[3] Rutherford, D., Graver, B., and Chen, C., "Noise and Climate Impacts of an Unconstrained Commercial Supersonic Network," International Council on Clean Transportation, 2019, https://theicct.org/sites/default/files/publications/Supersonic_Impact_Working_Paper_20190130.pdf [retrieved 6 June 2022].

[4] Peters, A., Spakovszky, Z. S., Lord, W. K., and Rose, B., "Ultrashort Nacelles for Low Fan Pressure Ratio Propulsors," *Journal of Turbomachinery*, Vol. 137, No. 2, 2015, Paper 021001. https://doi.org/10.1115/1.4028235

[5] Owens, R., Hasel, K., and Mapes, D., "Ultra High Bypass Turbofan Technologies for the Twenty-First Century," *26th Joint Propulsion Conference*, AIAA Paper 1990-2397, 1990. https://doi.org/10.2514/6.1990-2397

[6] Cumpsty, N., and Heyes, A., *Jet Propulsion*, Cambridge Univ. Press, Cambridge, England, U.K., 2015, pp. 191–194.

[7] Berton, J. J., Jones, S. M., Seidel, J. A., and Huff, D. L., "Noise Predictions for a Supersonic Business Jet Using Advanced Take-Off Procedures," *Aeronautical Journal*, Vol. 122, No. 1250, 2018, pp. 556–571. https://doi.org/10.1017/aer.2018.6

[8] Kharina, A., Macdonald, T., and Rutherford, D., "Environmental Performance of Emerging Supersonic Transport Aircraft," 2018, International Council on Clean Transportation, https://theicct.org/wp-content/uploads/2021/06/Environmental_Supersonic_Aircraft_20180717.pdf [retrieved 6 June 2022].

[9] Henne, P. A., "Case for Small Supersonic Civil Aircraft," *Journal of Aircraft*, Vol. 42, No. 3, 2005, pp. 765–774. https://doi.org/10.2514/1.5119

[10] "Environmental Technical Manual, Vol. I, Procedures for the Noise Certification of Aircraft. Document 9501; 2nd edition," Committee on Aviation Environmental Protection (CAEP) TR 9501 AN/929, 2015, https://www.icao.int/environmental-protection/Documents/SGAR.2015.ETM.Vol.1.pdf [retrieved 17 June 2023].

[11] "High-Speed Civil Transport Study," Boeing Commercial Airplanes, NASA CR-4233, Seattle, WA, 1990, https://ntrs.nasa.gov/citations/19890018277 [retrieved 11 May 2022].

[12] "Annex 16 to the Convention on International Civil Aviation Environmental Protection Volume 1: Aircraft Noise (Edition 8)," International Civil Aviation Organization (ICAO), 2017.

[13] Grantham, W. D., and Smith, P. M., "Development of SCR Aircraft Takeoff and Landing Procedures for Community Noise Abatement and their Impact on Flight Safety," Supersonic Cruise Res. 1979, Pt. 1, 1980, https://ntrs.nasa.gov/api/citations/19810009471/downloads/19810009471.pdf [retrieved 15 July 2023].

[14] "Notice for Proposed Rule Making: Noise Certification for Supersonic Airplanes (Docket No.: FAA-2020-0316; Notice No. 20-60)," Federal Aviation Administration, FAA TR 71, 2020, https://www.federalregister.gov/documents/2020/04/13/2020-07039/noise-certification-of-supersonic-airplanes [retrieved 11 May 2022].

[15] Falck, R. D., Ingraham, D., and Aretskin-Hariton, E., "Multidisciplinary Optimization of Urban-Air-Mobility Class Aircraft Trajectories with Acoustic Constraints," *2018 AIAA/IEEE Electric Aircraft Technologies Symposium (EATS)*, Inst. of Electrical and Electronics Engineers, New York, 2018, pp. 1–7. https://doi.org/10.2514/6.2018-4985

[16] Olson, E. D., "Advanced Takeoff Procedures for High-Speed Civil Transport Community Noise Reduction," *SAE Technical Papers*, Vol. 1, No. 921939, 1992, pp. 1612–1625. https://doi.org/10.4271/921939

[17] Baber, H. T., "Characteristics of the Advanced Supersonic Technology AST-105-1 Configured for Transpacific Range with Pratt and Whitney Aircraft Variable Stream Control Engines," NASA TM-7881, 1979, https://ntrs.nasa.gov/citations/19790015717 [retrieved 11 May 2022].

[18] Berton, J. J., "Variable Noise Reduction Systems for a Notional Supersonic Business Jet," *Journal of Aircraft*, Vol. 60, No. 3, 2023, pp. 688–701. https://doi.org/10.2514/1.C037019

[19] Filippone, A., "Aircraft Noise Prediction," *Progress in Aerospace Sciences*, Vol. 68, July 2014, pp. 27–63. https://doi.org/10.1016/j.paerosci.2014.02.001

[20] Kugelmann, B., "Minimizing the Noise of an Aircraft During Landing Approach," *Variational Calculus, Optimal Control and Applications*, Vol. 124, Nov. 1998, pp. 271–280. https://doi.org/10.1007/978-3-0348-8802-8_27

[21] Ohta, H., "Analysis of Minimum Noise Landing Approach Trajectory," *Journal of Guidance, Control, and Dynamics*, Vol. 5, No. 3, 1982, pp. 263–269. https://doi.org/10.2514/3.56166

[22] Udani, J. P., Mall, K., Grant, M. J., and Sun, D., "Optimal Flight Trajectory to Minimize Noise During Landing," *AIAA SciTech Forum–55th AIAA Aerospace Sciences Meeting*, AIAA Paper 2017-1180, 2017. https://doi.org/10.2514/6.2017-1180

[23] Abdallah, L., "Optimal Flight Paths Reducing the Aircraft Noise During Landing," *Communications in Computer and Information Science*, Vol. 14, Springer, Berlin, Heidelberg, 2008, pp. 1–10. https://doi.org/10.1007/978-3-540-87477-5_1

[24] Khardi, S., and Abdallah, L., "Optimization Approaches of Aircraft Flight Path Reducing Noise: Comparison of Modeling Methods," *Applied Acoustics*, Vol. 73, No. 4, 2012, pp. 291–301. https://doi.org/10.1016/j.apacoust.2011.06.012

[25] Bellman, R., *Dynamic Programming*, Princeton Univ. Press, Princeton, NJ, 2010, pp. 1–60.

[26] Gray, J. S., Hwang, J. T., Martins, J. R., Moore, K. T., and Naylor, B. A., "OpenMDAO: An Open-Source Framework for Multidisciplinary Design, Analysis, and Optimization," *Structural and Multidisciplinary Optimization*, Vol. 59, No. 4, 2019, pp. 1075–1104. https://doi.org/10.1007/s00158-019-02211-z

[27] Voet, L. J. A., Prakash, P., Speth, R. L., Sabnis, J. S., Tan, C. S., and Barrett, S. R. H., "Sensitivities of Aircraft Acoustic Metrics to Engine Design Variables for Multi-Disciplinary Optimization," *AIAA Journal*, Vol. 60, No. 8, 2022, pp. 4764–4774. https://doi.org/10.2514/1.J061411

[28] Falck, R., Gray, J., Ponnapalli, K., and Wright, T., "Dymos: A Python Package for Optimal Control of Multidisciplinary Systems," *Journal of Open Source Software*, Vol. 6, No. 59, 2021, p. 2809. https://doi.org/10.21105/joss.02809

[29] Berton, J. J., Huff, D. L., Seidel, J. A., and Geiselhart, K. A., "Supersonic Technology Concept Aeroplanes for Environmental Studies," *AIAA Scitech 2020 Forum*, AIAA Paper 2020-0263, Jan. 2020. https://doi.org/10.2514/6.2020-0263

[30] "Title 14: Aeronautics and Space—§25.111 Takeoff Path," Code of Federal Regulations, 2021, https://www.ecfr.gov/current/title-14/chapter-I/subchapter-C/part-25/subpart-B/subject-group-ECFR14f0e2fcc647a42/section-25.111#p-25.111 [retrieved 25 Sept. 2022].

[31] "Title 14: Aeronautics and Space—§91.117.a: Aircraft Speed," Code of Federal Regulations, 2022, https://www.ecfr.gov/current/title-14/chapter-I/subchapter-F/part-91/subpart-B/subject-group-ECFRe4c59b5f5506932/section-91.117# [retrieved 28 June 2023].

[32] Claus, R. W., Evans, A. L., Lylte, J. K., and Nichols, L. D., "Numerical Propulsion System Simulation," *Computing Systems in Engineering*, Vol. 2, No. 4, 1991, pp. 357–364. https://doi.org/10.1016/0956-0521(91)90003-N

[33] "ICAO Aircraft Engine Emissions Databank," 2021, European Union Aviation Safety Agency (EASA), https://www.easa.europa.eu/domains/environment/icao-aircraft-engine-emissions-databank [retrieved 22 April 2021].

[34] Prashanth, P., Voet, L. J. A., Speth, R. L., Sabnis, J. S., Tan, C. S., and Barrett, S. R. H., "Impact of Design Constraints on Noise and Emissions of Derivative Supersonic Engines," *Journal of Propulsion and Power*, Vol. 39, No. 3, 2023, pp. 454–463. https://doi.org/10.2514/1.B38918

[35] Mair, W. A., and Birdsall, D. L., *Aircraft Performance*, Vol. 5, Cambridge Univ. Press, Cambridge, England, U.K., 1996, pp. 119–161.

[36] McCullers, L. A., "Aircraft Configuration Optimization Including Optimized Flight Profiles," *NASA Langley Research Center Recent Experiences in Multidisciplinary Analysis and Optimization, Part 1*, 1984, pp. 395–412, https://ntrs.nasa.gov/citations/19870002310 [retrieved 11 May 2022].

[37] "Dymos Multidisciplinary Optimal Control Library: Optimal Control Transcriptions," The Dymos Development Team, 2022, https://openmdao.github.io/dymos/getting_started/transcriptions.html?highlight=collocation [retrieved 22 Aug. 2022].

[38] Herman, A. L., and Conway, B. A., "Direct Optimization Using Collocation Based on High-Order Gauss-Lobatto Quadrature Rules," *Journal of Guidance, Control, and Dynamics*, Vol. 19, No. 3, 1996, pp. 592–599. https://doi.org/10.2514/3.21662

[39] Lambe, A. B., and Martins, J. R., "Extensions to the Design Structure Matrix for the Description of Multidisciplinary Design, Analysis, and Optimization Processes," *Structural and Multidisciplinary Optimization*, Vol. 46, No. 2, 2012, pp. 273–284. https://doi.org/10.1007/s00158-012-0763-y

[40] Heidman, M. F., "Interim Prediction Method for Fan and Compressor Source Noise," NASA TR 71763, 1979, https://ntrs.nasa.gov/citations/19750017876 [retrieved 11 May 2022].

[41] Kontos, K. B., Janardan, B., and Gliebe, P., "Improved NASA-ANOPP Noise Prediction Computer Code for Advanced Subsonic Propulsion Systems," NASA TR 195480, 1996, https://ntrs.nasa.gov/citations/19960048499 [retrieved 11 May 2022].

[42] Hough, J. W., and Weir, D. S., "Aircraft Noise Prediction Program (ANOPP) Fan Noise Prediction for Small Engines," NASA CR-198300, 1996, https://ntrs.nasa.gov/citations/19960042711 [retrieved 11 May 2022].

[43] Kontos, K., Kraft, R., and Gliebe, P., "Improved NASA-ANOPP Noise Prediction Computer Code for Advanced Subsonic Propulsion Systems Volume 2: Fan Suppression Model Development," NASA CR-202309, 1996, https://ntrs.nasa.gov/citations/19970005047.

[44] Emmerling, J. J., "Core Engine Noise Control Program Volume III, Supplement I—Prediction Methods," Aircraft Engine Group General Electric Company TR 125, Cincinnati, OH, 1976, https://apps.dtic.mil/sti/pdfs/ADA030376.pdf [retrieved 11 May 2022].

[45] "SAE ARP876-F Gas Turbine Jet Exhaust Noise Prediction," SAE Aerospace, Soc. of Automotive Engineers ARP876-F, 2021, https://www.sae.org/standards/content/arp876f/ [retrieved 17 June 2023].

[46] Fink, M. R., "Airframe Noise Prediction Method," Dept. of Transportation FAA-RD-77-29, 1977, https://www.tc.faa.gov/its/worldpac/techrpt/rd77-29.pdf [retrieved 11 May 2022].

[47] Rawls, J. W., and Yeager, J. C., "High Speed Research Noise Prediction Code (HSRNOISE) User's and Theoretical Manual," NASA TR 2004-213014, Hampton, VA, 2004, https://ntrs.nasa.gov/citations/20040200978 [retrieved 11 May 2022].

[48] "SAE ARP866-B Standard Values of Atmospheric Absorption as a Function of Temperature and Humidity," SAE Aerospace, Soc. of Automotive Engineers ARP866-B, 2012, https://www.sae.org/standards/content/arp866b/ [retrieved 17 June 2023].

[49] Chien, C. F., and Soroka, W. W., "Sound Propagation Along an Impedance Plane," *Journal of Sound and Vibration*, Vol. 43, No. 1, 1975, pp. 9–20. https://doi.org/10.1016/0022-460X(75)90200-X

[50] "SAE AIR5662 Method for Predicting Lateral Attenuation of Airplane Noise," SAE Aerospace, Soc. of Automotive Engineers AIR5662, 2019, https://www.sae.org/standards/content/air5662/ [retrieved 17 June 2023].

[51] *Aircraft Tire Data Book*, The Goodyear Tire & Rubber Company, 2001, https://web.archive.org/web/20120913132818/http://www.goodyearaviation.com/resources/pdf/db_airdatabook.pdf [retrieved 8 July 2022].

[52] Wächter, A., and Biegler, L., "On the Implementation of an Interior-Point Filter Line-Search Algorithm for Large-Scale Nonlinear Programming," *Mathematical Programming*, Vol. 106, No. 1, 2006, pp. 25–57. https://doi.org/10.1007/s10107-004-0559-y

[53] Revels, J., and Pearson, J., "ReverseDiff.jl," 2016, https://github.com/JuliaDiff/ReverseDiff.jl [retrieved 11 May 2022].

[54] Grodzevich, O., and Romanko, O., "Normalization and Other Topics in Multi-Objective Optimization," *Proceedings of the Fields-MITACS Industrial Problems Workshop (Toronto, Canada)*, The Fields Inst., Toronto, Canada, 2006, pp. 89–101, http://miis.maths.ox.ac.uk/miis/233/1/fmipw1-6.pdf [retrieved 22 July 2023].

[55] Boyd, S. P., and Vandenberghe, L., *Convex Optimization*, Cambridge Univ. Press, Cambridge, England, U.K., 2004, pp. 215–273.

[56] Martins, J. R., and Ning, A., *Engineering Design Optimization*, Cambridge Univ. Press, Cambridge, England, U.K., 2021, pp. 210–213.

[57] "Views of the United States on Supersonic Aircraft Noise Future Work during the CAEP/13 Cycle," Committee on Aviation Environmental

Protection (CAEP), 2022, https://icao.usmission.gov/wp-content/uploads/sites/280/CAEP.12.WP_.064.16.en-VIEWS-OF-THE-UNITED-STATES-ON-SUPERSONIC-AIRCRAFT-NOISE-FUTURE-WORK-DURING-THE-CAEP13-CYCLE.pdf [retrieved 25 June 2023].

[58] Bridges, J. E., Stephens, D., and Berton, J. J., "Quantifying Uncertainty of Landing and Takeoff Noise for Commercial Supersonic Aircraft," *28th AIAA/CEAS Aeroacoustics 2022 Conference*, AIAA Paper 2022-3051, 2022. https://doi.org/10.2514/6.2022-3051

[59] Henderson, B. S., Huff, D. L., and Berton, J. J., "Jet Noise Prediction Comparisons with Scale Model Tests and Learjet Flyover Data," *25th AIAA/CEAS Aeroacoustics Conference*, AIAA Paper 2019-2768, 2019. https://doi.org/10.2514/6.2019-2768

[60] Bridges, J. E., "Diagnosing Noise Features of Internally Mixed, External Plug Exhaust Systems," *AIAA Aviation 2023 Forum*, AIAA Paper 2023-3210, 2023. https://doi.org/10.2514/6.2023-3210

[61] Berton, J. J., "Simultaneous Use of Ground Reflection and Lateral Attenuation Noise Models," *Journal of Aircraft*, Vol. 59, No. 2, 2022, pp. 536–543. https://doi.org/10.2514/1.C036488

[62] Smith, M., "Aircraft Noise Measurement–Alternatives to the Standard 1.2 Metres Microphone Height," *10th Aeroacoustics Conference*, AIAA Paper 1986-1960, 1986. https://doi.org/10.2514/6.1986-1960

[63] Albert, M., Bousquet, P., and Lizarazu, D., "Ground Effects for Aircraft Noise Certification," *23rd AIAA/CEAS Aeroacoustics Conference*, AIAA Paper 2017-3845, 2017. https://doi.org/10.2514/6.2017-3845

[64] Nesbitt, E., Lan, J., and Hunkler, S., "Microphone Acoustic Characteristics for Aircraft Flyover Testing," *AIAA Aviation 2020 Forum*, AIAA Paper 2020-2613, 2020. https://doi.org/10.2514/6.2020-2613

[65] "U.S. Standard Atmosphere, 1976," National Oceanic and Atmospheric Administration, NASA, United States Air Force, U.S. Government, NASA-TM-X-74335, 1976, p. 241, https://ntrs.nasa.gov/citations/19770009539 [retrieved 11 May 2022].